Typeset using LaTeX **twocolumn** style in AASTeX631

Draft version October 1, 2025

Photometric Redshift Forecast for 7-Dimensional Sky Survey

Eunhee Ko (고은희),[1,2] Myungshin Im,[1] Yujin Yang,[3] Ji Hoon Kim,[1] Seong-Kook Lee,[1] and Gregory S.-H. Paek[1]

[1]*SNU Astronomy Research Center, Astronomy Program, Department of Physics and Astronomy, Seoul National University, 1 Gwanak-ro, Gwanak-gu, Seoul 08826, Republic of Korea*

[2]*Institut d'Astrophysique de Paris, UMR 7095, CNRS, Sorbonne Université, 98 bis boulevard Arago, F-75014 Paris, France*

[3]*Korea Astronomy and Space Science Institute, Daedeokdae-ro 776, Yuseong-gu Daejeon 34055, Republic of Korea*

ABSTRACT

We investigate the expected accuracy of redshifts that can be obtained using low-resolution spectroscopic (medium-band) data from the 7-Dimensional Sky Survey (7DS). By leveraging 40 densely sampled filters with widths of full width at half maximum (FWHM) = 25 nm, we create 7DS mock catalogs and estimate the redshift accuracy for three 7DS main surveys: Wide-field Time-Domain Survey (WTS), Intensive Monitoring Survey (IMS), and Reference Image Survey (RIS). Using photometric redshifts calculated from EAZY, we find that the five-year WTS provides reliable photometric redshifts with an normalized median absolute deviation ($\sigma_{\rm NMAD}$) ranging from 0.003 to 0.007 and a catastrophic failure fraction (η) from 0.8% to 8.1% at $19 \leq m_{625} < 22$. The spectral resolution $R \sim 50$ of the medium-band dataset effectively captures the 4000 Å break and various emission lines. We also explore the synergy with data obtained from Pan-STARRS1, VIKING, and SPHEREx surveys. Combining the SPHEREx all-sky data with WTS significantly improves the accuracy of photometric redshift estimates, achieving $\eta = 0.4\%$ and $\sigma_{\rm NMAD} = 0.004$ for fainter sources at higher redshifts. The additional near-IR information provided by SPHEREx and VIKING plays an essential role in resolving degeneracies between low and high redshifts. We also observe color excesses by subtracting adjacent broad-band data, which improves the confinement of photometric redshifts and aids in the detection of strong emission line galaxies.

Keywords: Medium band photometry (1021) — Redshift surveys (1378) — Sky surveys (1464)

1. INTRODUCTION

In extragalactic astronomy, the distribution of galaxies provides crucial insights into the evolution of matter in the universe. A fundamental quantity for measuring their distances is redshift, which reveals how the wavelength of light from an extragalactic source is stretched due to the expansion of the universe. A rich dataset of redshifts allows us to infer extensively the galaxy demographics and related astrophysical phenomena, including star formation (e.g., Arnouts et al. 2005; Karim et al. 2011; Finkelstein et al. 2015; Bouwens et al. 2021), feedback (e.g., Simpson et al. 2013; Best et al. 2014; Ruppin et al. 2023), and dust attenuation (e.g., Finkelstein et al. 2010; Cucciati et al. 2012; Burgarella et al. 2013) over the evolution of the universe. Furthermore, observational cosmology is another testbed that operates with redshifts. In this regard, robust photometric redshift samples provide a comprehensive picture of the universe. In the standard cosmological model, the primary goal is to minimize any uncertainties as much as possible and to resolve the current tension (e.g., Allen et al. 2011; The LSST Dark Energy Science Collaboration et al. 2018; Mandelbaum 2018; Stölzner et al. 2021; Abbott et al. 2022).

From a classical point of view, determining the redshift of galaxies involves spectroscopy. Spectral features, such as emission lines and breaks, allow us to calculate the degree of shift in the spectra of galaxies. Although spectroscopic observations provide distance information with high fidelity, they are also time-consuming, expensive, and susceptible to low signal-to-noise ratios (S/N), particularly for faint and distant sources. As an alternative, *photometric redshifts* (photo-z) are instrumental in deriving the redshift of a large number of samples based on multi-photometric data. Serving as proxies for low-resolution spectra, photometric redshifts complement the expenses associated with spectroscopic ob-

Corresponding author: Myungshin Im
myungshin.im@gmail.com

servations (e.g., Laigle et al. 2016; Alarcon et al. 2021; Weaver et al. 2022). Since the concept of photometric redshifts was first suggested in 1960s (Baum 1962; Koo 1985; Loh & Spillar 1986; Bolzonella et al. 2000), we can now derive photometric redshifts in the deeper reaches of the universe with the availability of large-sky survey (Salvato et al. 2019; Newman & Gruen 2022 for a recent review). Moreover, they are and will continue to be employed to constrain cosmological probes and investigate astrophysical phenomena in a more statistically robust way. However, despite their advantages, uncertainties of photometric redshifts arising from intrinsically low resolution and contamination still persist as significant challenges.

A novel observational strategy, known as *photo-spectra*, offers a solution to the challenges posed by both low S/N and spectral resolution in previous redshift measurement methods. Functioning as quasi-spectra, the higher spectral resolution achieved through medium- and narrow-band filters enables us to catch the spectral features more precisely, otherwise not resolvable in broad-band filters (e.g., Wolf et al. 2003; Cardamone et al. 2010; Benitez et al. 2014; Hernán-Caballero et al. 2021; Navarro-Gironés et al. 2023). Although it does not reach the full precision of spectroscopic redshifts, this approach can achieve high S/N with relatively short integration time—typically only a few minutes per filter while simultaneously observing thousands of targets within the field of view (e.g., Bonoli et al. 2021)—in contrast to spectroscopic surveys, which generally require 1–3 hours per object (e.g., Davis et al. 2003). Unlike spectroscopy, it eliminates the need for a specific target selection process. Furthermore, imaging data, analogous to an integral field unit (IFU) observations, allow the spatially-resolved analysis of nearby galaxies (Benitez et al. 2014; González Delgado et al. 2021).

Over the past two decades, a few medium- or narrow-band surveys covering moderately large fields—given the constraints of medium-band surveys, which require more integration time than broad-band surveys—have been conducted. The Classifying Objects by Medium-Band Observations in 17 Filters (COMBO-17, Wolf et al. 2003) survey pioneered the medium-band surveys, whose filter sets provide spectral resolutions of $R = 10$–20 and 1–2% of photometric redshift accuracies. With 5 broad-band filters (UBVRI) and 12 medium-band filters, spanning 400 nm to 930 nm across three fields over an area of 0.78 $\deg^2$, produced reliable photometric redshifts with normalized median absolute deviation of $\sigma_{\rm NMAD} \approx 0.03$ for a sample of $\sim 25{,}000$ galaxies.

Similarly, the Multi-wavelength Survey by Yale-Chile (MUSYC, Taylor et al. 2009; Cardamone et al. 2010) is a deep 18-band optical medium-band survey over the $30' \times 30'$ Extended Chandra Deep Field-South. MUSYC combines Subaru medium-band images with existing Subaru $UBVRIzJHK$ from Garching-Bonn Deep Survey (GaBoDS, Hildebrandt et al. 2006), as well as data from ESO (Moy et al. 2003), and SIMPLE (Damen et al. 2011). This integration results in an improvement in redshift accuracy up to $\sigma_{\rm NMAD} \sim 0.008$ for the entire sample with $m_R < 25.3$. Notably, the addition of deeper medium-band filter data increases the number of fainter sources and reduces the scatter of photometric redshifts. For near-IR observations, the NOAO Extremely Wide-Field Infrared Imager (NEWFIRM, Whitaker et al. 2011) employs near-IR medium-band filter systems covering 1.0 μm to 1.8 μm, including $J1, J2, J3, H1, H2$, and K (van Dokkum et al. 2009). These filters are designed to probe the Balmer and Lyman break at $1.5 < z < 3.5$. Photometric redshifts from NEWFIRM are in good agreement with spectroscopic redshifts ($\sigma_{\rm NMAD} \sim 0.008$ to ~ 0.017).

More recently, the Javalambre-Physics of the Accelerating Universe Astrophysical Survey (J-PAS, Benítez et al. 2009a; Benitez et al. 2014) aims at observing the Northern sky with 54 narrow-band filters with 145 Å widths covering 3785–9000 Å. For a precursory survey to estimate the scientific feasibility of J-PAS, MiniJ-PAS (Bonoli et al. 2021) demonstrates that a combination of 54 narrow-band filters and 6 broadband filters yields highly reliable photometric redshifts ($\sigma_{\rm NMAD} < 0.003$) at $m_r < 23$ and *odds* > 0.82 (Hernán-Caballero et al. 2021).[1] Additionally, it is shown that further improvement in photo-z calculation is expected with the addition of Spectral Energy Distribution (SED) templates capturing the survey features (Laur et al. 2022). The potential of their narrow-band systems extends from the local universe (e.g., S-PLUS, Mendes de Oliveira et al. 2019; J-PLUS, Cenarro et al. 2019) to high-precision photo-z surveys (e.g., PAUS, Benítez et al. 2009b; Navarro-Gironés et al. 2023).

The previous efforts of obtaining quasi-spectra with medium- or narrow-bands are not without limitations. The field of view of many of the aforementioned surveys is rather limited at $\ll 1 \deg^2$. Also, previous attempts utilize a filter wheel or its equivalent, so that simultaneous coverage of all the spectral elements is not possible. Overcoming these weaknesses is important considering the advancement of multi-messenger astronomy and transient surveys, where the discovery and charac-

[1] Here, the *odds* parameter refers to the integrated posterior probability within a chosen interval around the best-fit photo-z; See Benítez (2000) for details.

terization of rapidly evolving transients in a large search area is key to success (Abbott et al. 2017; Kim et al. 2021; Paek et al. 2024).

To overcome the shortcomings of previous works, we have been building the 7-Dimensional Telescope (7DT), a multiple telescope system with twenty 0.5 m wide-field telescopes in Chile (Im et al. 2023; Kim et al. 2024; Im et al. in preparation). By having each wide-field telescope observe at different wavelengths, 7DT enables a nearly simultaneous spectral mapping of the sky over a wide field of view (~ 1.2 deg^2) with 40 medium-band filters that cover from 400 nm to 900 nm. The main focus of the project is to rapidly identify the optical counterpart of gravitational wave (GW) sources with its spectral mapping capability (Im et al. 2023).

Given the power of the all-sky medium-band filters in 7DT, we plan to carry out the 7-Dimensional Sky Survey (7DS) and provide spectral maps of the universe at different depths and time cadence to tackle various scientific topics. The 7DS survey aims to unveil various problems spanning multi-messenger astronomy, supermassive black holes, active galactic nuclei (AGN), galaxy evolution, cosmology, the Milky Way galaxy, transients, solar system objects, and exoplanets. The 7DS will be made of three surveys: *Reference Imaging Survey* (RIS) - all-sky spectral mapping survey to a depth of ~ 20 AB mag for a point source detection; *Wide-field Time-Domain Survey* (WTS) - a two-week cadence time-series spectral mapping of a 1,000 deg^2 area; and *Intensive Monitoring Survey* (IMS) - daily spectral monitoring of about a 10 deg^2 field. The stacked images of the time series observations by IMS and WTS can reach about 2 and 3 magnitudes deeper than RIS, respectively.

The scientific potential of the 7DS can be maximized when combined with existing or upcoming surveys. For instance, SPHEREx (Spectro-Photometer for the History of the Universe, Epoch of Reionization, and Ices Explorer, Doré et al. 2014) is a space mission to probe the all-sky that can obtain a low-resolution spectral map in the near-IR wavelength range of 0.75–5.0 μm. Other existing and future missions, such as the Pan-STARRS1 (Chambers et al. 2016), VISTA surveys (Arnaboldi et al. 2007; Edge et al. 2013), and Euclid (Laureijs et al. 2011), can provide complementary datasets for 7DS.

In this paper, we evaluate the performance of photometric redshifts of the three different surveys of 7DS. Our analysis includes exploring the use of upcoming data and its synergy with other surveys, preparing for the maximization of their combined power. The structure of this paper is as follows. Section 2 outlines the overall background and scientific goals of the 7DS's surveys. In Section 3, we detail the process of building mock data for the 7DS, featuring 40 medium-band filters, and for other systems such as Pan-STARRS1, VIKING, and SPHEREx survey. Forecasts of photometric redshifts obtained from the 7DS and their synergy with other surveys are described in Section 4 and Section 5, respectively. Section 6 discusses the potential of 7DS for tracing spectral features and highlights further improvements through the inclusion of near-IR information, with particular emphasis on the advantages of its distinctive medium-band system. The conclusion is summarized in Section 7. Throughout the paper, the AB magnitude system is adopted (Oke 1974).

2. 7DS IN A NUTSHELL

7DS is a multi-purpose survey designed to perform time-series, wide-field, spatially resolved spectroscopy of the sky, utilizing the nearly simultaneous 40 medium-band imaging capability of the 7DT telescope. 7DT will produce low-resolution spectra for all pixels in the field of view. The two main objectives of the survey are (1) to identify optical counterparts and host galaxies of GW sources, and (2) to characterize the spectral variability of variable sources in the Universe.

Reference Imaging Survey—For the first objective, we will conduct rapid target-of-opportunity spectral mapping of GW source localization regions. The spectral mapping capability of 7DT integrates wide-field imaging and spectroscopy, allowing for efficient identification of kilonovae. To support this effort, we will carry out the RIS, a spectral imaging survey covering 22,000 deg^2 of the sky at Dec $< +20^\circ$. It will reach wavelength-dependent depths of 20 AB mag at 400 nm and 18 AB mag at 875 nm for point-source detection at the 5σ level. RIS images will serve as reference frames to detect new transients and extract their spectra.

In addition, RIS data will be used to construct galaxy ($z \lesssim 0.5$) and quasar ($z \lesssim 3$) catalogs, which can support statistical inference of host galaxies or active galactic nuclei (AGNs) for GW sources lacking clear optical counterparts. Our goal is to measure redshifts with an accuracy of 1% for sources a few tenths of a magnitude brighter than the survey's limiting magnitude, and a few tenths of a percent when significantly brighter than the magnitude limit. This level of redshift precision is several times better than typical photometric redshifts from broad-band surveys and is necessary for distinguishing galaxy cluster-scale structures without confusion from foreground or background objects (e.g., Ivezić et al. 2019; Euclid Collaboration et al. 2020; Graham et al. 2020).

Wide-field Time-Domain Survey—The second component, the WTS, will monitor spectral variability across up to 8,000 $\deg^2$ with a cadence of approximately 20 days. A primary target is AGNs, whose long-term (> months) spectral variability can be used to estimate the masses of supermassive black holes via reverberation mapping. The depth of single-epoch WTS data will match that of RIS, but stacking data over the five-year survey will yield a depth of 22 AB mag (400 nm) for point-source detection. These deep stacked data will facilitate studies of large-scale structures (e.g., galaxy clusters) and galaxy evolution across environments. As with RIS, we require redshift accuracy for galaxies and quasars comparable to that of RIS, but at a fainter magnitude limit. With its wide-area coverage and highly accurate redshifts, WTS is comparable to the J-PAS survey (Benítez et al. 2009a; Benitez et al. 2014), a Stage-IV cosmological survey (Beltrame et al. 2024). We hope to deliver cosmological parameters with comparable precision, if not better, with J-PAS.

Intensive Monitoring Survey—Finally, the IMS is a daily-cadence spectral mapping program of a ~20 $\deg^2$ area near the South Ecliptic Pole. Like WTS, its single-epoch depth will match that of RIS, while the five-year stacked depth will reach 23 AB mag (400 nm) for point-source detection. IMS will track short-term spectral variability of sources such as AGNs, and its stacked data will enable deeper probing of the Universe's large-scale structure.

3. MOCK CATALOG GENERATION

We start the construction of the 7DS mock catalog by using the model SED catalog from EL-COSMOS (Saito et al. 2020). EL-COSMOS is a mock SED catalog based on COSMOS2015 photometric catalog (Laigle et al. 2016), covering the COSMOS field uniformly with 31 photometric bands from near ultraviolet to mid-IR (2000 Å to 10^5 Å). This extensive coverage enables the modeling of a homogeneous galaxy population to probe spectral features such as emission lines. As a result, based on the accurate photo-zs, verified with spectroscopic redshifts (see Laigle et al. 2016 for further details), the EL-COSMOS provides representative samples of 518,404 galaxies, reliably spanning a redshift range of $0 \lesssim z \lesssim 2.5$.

The SED modeling process, outlined by Saito et al. (2020), involves building the stellar continuum spectrum based on the same procedure in Ilbert et al. (2015) and Laigle et al. (2016). They adopted a stellar population synthesis model from Bruzual & Charlot (2003, BC03) and an initial mass function from Chabrier (2003). Using the SED fitting calculation with `LePhare`, final SED models are determined as the best-fit template with the minimum χ^2. The luminosity and wavelength are corrected by adopting photometric redshifts from COSMOS2015 as the true values. Star-forming nebular regions (continuum emission and discrete emission lines) are added following the approach by Schaerer & de Barros (2009). The number of Lyman continuum photons, $Q_{\rm LyC}$, is obtained from the integrated luminosity of the BC03 spectra and converted to the luminosity of discrete emission lines ([OII] 3728 Å, H_β 4863 Å, [OIIIa] 4959 Å, [OIIIb] 5007 Å, and H_α 6565 Å). The modeled SED aligns with the empirical relation between star-formation rate and H_α luminosity based on the link between intrinsic emission line luminosities and the number of ionizing photons (Kennicutt & Evans 2012). Furthermore, intrinsic emission line luminosities and dust attenuation are calibrated by taking advantage of matched spectroscopic samples from zCOSMOS-Bright (Lilly et al. 2007) and 3D-HST (Brammer et al. 2012; Momcheva et al. 2016) to match the observed emission lines. On the basis of observations from zCOSMOS-Bright and 3D-HST, a stellar-to-nebular extinction ratio dependent on redshift evolution was derived and applied to the model SEDs.

3.1. *7DS Mock Catalog*

We generate mock transmission curves for the 40 medium-band filters by starting from a smoothed top-hat transmission curve with a FWHM of 25 nm. To replicate realistic transmission curves as in observation, we incorporate the efficiencies of the telescope, detector, and atmospheric transmission given in Table A.1 (Im et al. in preparation). The combined telescope efficiency is convolved with atmospheric transmission,[2] assuming observational conditions similar to those at the Paranal Observatory, where the Very Large Telescope is located. Given the goal of the prediction study and uncertainties in practical observational conditions, we confirm that this assumption does not affect the results throughout the analysis. The resulting filter transmission curves are presented in the top panel of Figure 1. Hereafter, we denote the magnitude observed at a filter with a central wavelength of λ nm as m_λ (e.g., m_{625} for the magnitude at the 625 nm filter).

Note that we do not include the effect of foreground Galactic extinction in our mock photometry for the following reasons: (1) The COSMOS2015 catalog, from which our mocks are built, has already been corrected for Galactic extinction, thereby removing extinction-

[2] https://www.eso.org/sci/software/pipelines/skytools/skycalc

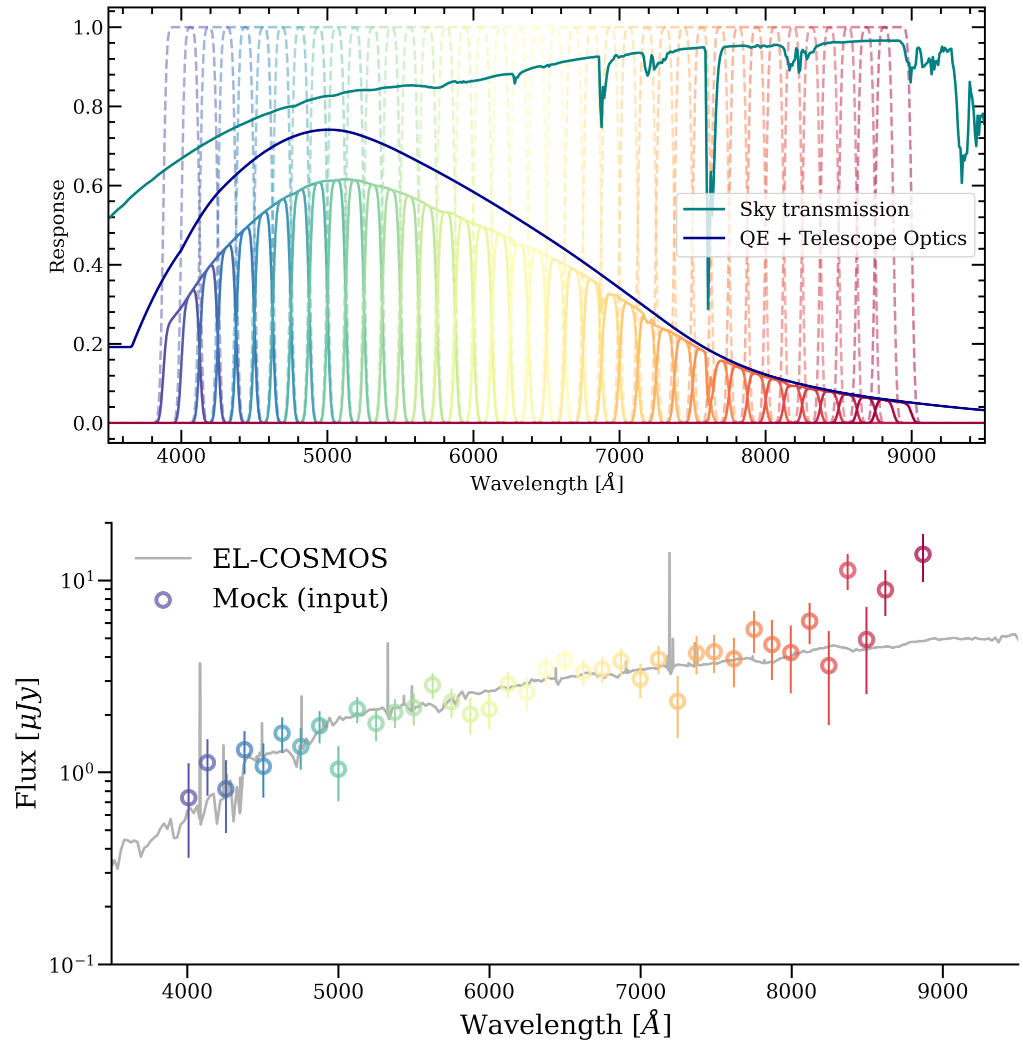

Figure 1. Top panel: Simulated filter transmission curves. Bottom panel: An example of EL-COSMOS SED (gray line) and its 7DS-like mock (data points).

induced flux biases from our predictions. (2) In practice, the variation of foreground Galactic extinction across the $\sim$2 deg^2 COSMOS field is small and difficult to extrapolate to wide-field surveys. The original COSMOS2015 catalog applied extinction corrections using the extinction curve from Allen (1976) and the dust map from Schlegel et al. (1998), with Galactic reddening E_{B-V} along the line of sight ranging from 0.020 to 0.030 (Galametz et al. 2017). Near the limiting magnitude of the WTS (see Table 1), this level of E_{B-V} error is subdominant to the 1σ photometric error ($\sim \pm 0.2$), though it may be non-negligible for brighter samples. Such uncertainties could bias the colors of nearby galaxies, and therefore degrade the overall photo-z accuracy across all redshift ranges (Bordoloi et al. 2010; Galametz et al. 2017). To limit the scope of our study as a proof-of-concept, we assume that Galactic extinction does not impact our estimate significantly, while it must be carefully treated in real observations.

Next, we calculate the photometric fluxes detected in the simulated filter windows by using the `trapezoid` function in `scipy.integrate`. The wavelength step of the transmission curve is set to 1 nm, which corresponds to the wavelength resolution of EL-COSMOS. This choice ensures accurate flux calculations without missing important spectral features, considering the FWHM of 7DS medium-band filters (25 nm). Flux errors are determined as a function of exposure time, using the Eq. (1), with the exposure time set to a five-year observation scenario of WTS (hereafter WTS Y5) and assuming 70% available observation time (180 seconds with 14 days cadence for 5 years and 70% observation efficiency =15,600 seconds). For the IMS Y5 and RIS, we scaled the exposure time to 156,000 seconds and 600 seconds, respectively, by considering the same condition and different cadence, and using

$$\mathrm{S/N} = \frac{Q_{\mathrm{source}}}{\sqrt{Q_{\mathrm{source}} + Q_{\mathrm{sky}} + Q_{\mathrm{dark}} + Q^2_{\mathrm{readout}}}}, \quad (1)$$

where Q_{source} is the number of photons received from the target source during the given exposure time, Q_{sky} from the background sky, Q_{dark} from the dark current of the detector, and Q_{readout} from readout noise.

Lastly, we introduce random noise following a normal distribution with a standard deviation of the true flux error to each flux point. We calculate the 5σ depth as the limiting magnitude, at which the S/N from Eq. (1) equals 5 for each filter set. As a fiducial reference filter, we choose m_{625}, whose central wavelength is comparable to the standard broad R-band filter and provides robust S/N. The overall 5σ depths of the simulated RIS, WTS Y5, and IMS Y5 are 20.83, 22.62, and 23.88 respectively at m_{625}. Of the 518,404 sources in the EL-COSMOS catalog, 20,654 galaxies are brighter than the WTS Y5 depth.

It is crucial to emphasize that these samples represent the observed data as an ensemble of realizations. An illustrative example of the EL-COSMOS SED and final photometric mock is depicted in the bottom panel of Figure 1.

3.2. *SPHEREx Mock Catalog*

One of our primary objectives in leveraging the spectral resolution of medium-bands is to enhance their effectiveness in deriving accurate photometric redshifts with a combination of other complementary surveys. In this context, SPHEREx can bridge the information gap between the optical and near-IR wavelength while maintaining a similar spectral resolution. Figure 2 illustrates the redshift window that can be probed by 7DS and other surveys.

The notable feature of SPHEREx is Linear Variable Filter (LVF) that is built to shift the pointings in small and consecutive steps. This enables spectroscopic observations without the need for a traditional spectrometer and effective mapping of the sky in terms of both time and field of view. Since the LVFs of SPHEREx capture different central wavelengths as the telescope pointing moves, they are different from fixed bandwidth filters in practice. However, for simplicity, we treat LVFs as 96 photometric filter systems based on previous SPHEREx prediction studies.[3] We follow the same procedure as in 7DS except for ignoring sky transmission and applying the SPHEREx instrumental parameters from Doré et al. (2014). Also, we set the exposure time for the 2 years of SPHEREx all-sky (shallow) survey. The resulting depths range between 19.59 and 17.84 magnitudes over the wavelength range of 0.75 to 5.0 μ m.[4] For simplicity, we refer to the data from the SPHEREx all-sky survey as "SPHEREx".

3.3. *Pan-STARRS1 and VIKING Mock Catalogs*

We also create mock catalogs for two currently existing surveys: Panoramic Survey Telescope and Rapid Response System (Pan-STARRS1, Chambers et al. 2016) and VISTA Kilo-Degree Infrared Galaxy (VIKING, Arnaboldi et al. 2007; Edge et al. 2013). This set of choices is to assess the impact of incorporating broad-band optical filters with high S/N and near-IR information. Instead of generating new transmission curves similarly in the 7DS and SPHEREx mock, we use the transmission curves provided by the Pan-STARRS (Tonry et al. 2012) and VIKING (Arnaboldi et al. 2007) photometric systems to calculate fluxes. To determine the photometric magnitude error σ_{err}, we adopt a conversion from 5σ limiting magnitude m_{lim} and observed magnitude m_{obs} obtained from the calculated flux, as suggested in Sesar et al. (2007) and Ivezić et al. (2019),

$$\sigma^2_{\mathrm{err}} = (0.04 - \gamma)x + \gamma x^2, \quad (2)$$

where $x = 10^{0.4(m_{\mathrm{obs}} - m_{\mathrm{lim}})}$ and $\gamma = 0.04$. Here γ refers to a factor dependent on possible noise sources, such as sky brightness and/or readout noises. By setting $\gamma = 0.04$, we assume that these effects are properly processed with little systematic errors after calibration (e.g., Graham et al. 2018, 2020; Euclid Collaboration et al. 2020).

We adopt Pan-STARRS1 (PS1) m_{lim} values (g, r, i, z, y; AB magnitude) as (23.3, 23.2, 23.1, 22.3, 21.4) from Chambers et al. (2016). The photometric system of VIKING is originally given in Vega magnitude, so we convert its m_{lim} values (z, Y, J, H, K_s) described in Barnett et al. (2021) to AB counterparts (22.1, 20.3, 20.9, 19.8, 19.2).[5] Finally, we introduce random error to the true flux, same as in the 7DS and SPHEREx mock.

We summarize the overall survey depths used in our study in Table 1.

[3] While SPHEREx changed the number of LVF channels to 102, we assume that this modification is negligible in the proof-of-concept study as discussed in Cheng & Chang 2022.

[4] https://github.com/SPHEREx/Public-products

[5] http://casu.ast.cam.ac.uk/surveys-projects/vista/technical/filter-set/

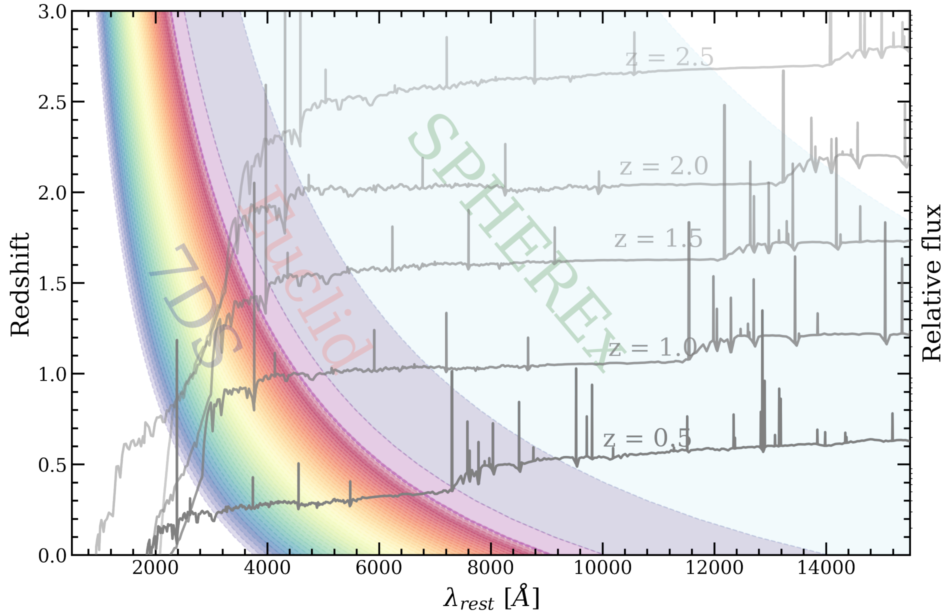

Figure 2. An illustration of the redshifted spectral energy distribution at $z = 0.5, 1.0, 1.5, 2.0, 2.5, 3, 0$ and wavelength window filters from 7DS (40 medium-band filters, 4000–8875 Å), Euclid (J and H) and SPHEREx (96 LVFs, 0.75–5.0 μm) as a function of redshifts.

Table 1. 5σ magnitude depth in 7DS, PS1, VIKING, and SPHEREx

Surveys	Filter	5σ limiting magnitude		
7DS		RIS	WTS Y5	IMS Y5 [a]
	m_{400}	21.17	22.99	24.24
	m_{413}	21.22	23.02	24.27
	m_{425}	21.31	23.11	24.37
	m_{438}	21.33	23.13	24.38
Pan-STARRS1	g	23.3 [b]		
	r	23.2		
	i	23.1		
	z	22.3		
	y	21.4		
VIKING	z	22.1 [b]		
	Y	20.3		
	J	20.9		
	H	19.8		
	K_s	19.2		
SPHEREx	0.75 [c]	19.59 [a]		
	0.77	19.58		
	0.79	19.56		
	0.81	19.55		
	0.83	19.54		

Table 1 *continued*

Table 1 *(continued)*

Surveys	Filter	5σ limiting magnitude

[a] 5σ depth in $m_{\rm AB}$ at which S/N = 5 computed on the customized filter curves for the point source detection (see Section 3.1–3.2).

[b] Same 5σ depth as (a), but computed on the actual filter curve (see Section 3.3).

[c] Central wavelength in μm. Note that SPHEREx is not filter-based but LVFs system.

Note—Only a portion of this table is shown here. The full version of the table is available in the online supplementary material.

3.4. *Photometric Redshift: EAZY*

We use the `EAZY` code for calculating photometric redshifts (Brammer et al. 2008). `EAZY` is an optimized tool that employs template fitting and a Bayesian approach to determine photometric redshifts efficiently. The templates from `EAZY` are constructed based on the PEGASE models (Fioc & Rocca-Volmerange 1997), which comprise ~ 3000 spectra spanning ages from 1 Myr to 20 Gyr with diverse star formation histories. In this work, we use the `eazy_v1.3` template set, where emission lines are added following the prescription of Ilbert et al. (2009).

From these input templates, the *nonnegative matrix factorization* (NMF) algorithm (Blanton & Roweis 2007) can find an optimized group of templates and template error function, reducing calculation time in the absence of spectroscopic samples (see Brammer et al. 2008 for more details). This feature aligns with our study's purpose of probing the photometric information through iterative experiments. However, considering the survey's wide-ranging data and advancing technologies, maximizing its potential is crucial. We leave future improvements to obtain more accurate photometric redshifts for our future study.

Among various point estimates of $z_{\rm phot}$ provided by `EAZY`, we adopt `z_a` unless otherwise specified (e.g., application of priors). This estimate corresponds to the redshift that minimizes χ^2 from linear combinations of all templates, without applying any prior. In our tests for the non-prior case, `z_a` yields better photo-z performance than `z_m1`, which marginalizes over the Gaussian likelihood function $\exp\left(-\chi^2\right)$. Moreover, `z_a` directly links the photometric measurements to their best-fitting templates, making it a natural choice for our analysis.

To explore the potential for future improvements, we further investigate improvements by applying an apparent magnitude prior. For the results obtained with the inclusion of priors, we adopt `z_m2`, which has been shown to provide the best photo-z estimate with priors (Brammer et al. 2008). Following Benítez (2000), the apparent magnitude prior $p(z|m_{625})$ is customized by fitting the redshift distribution of galaxies within a given magnitude bin $m_{625,i}$ to the functional form:

$$p(z|m_{625,i}) \propto z^{\gamma_i} \exp\left[-(z/z_{0,i})^{\gamma_i}\right], \qquad (3)$$

where γ_i and $z_{0,i}$ are fitting parameters and i denotes the i-th galaxy in the catalog. The priors are determined by dividing the EL-COSMOS sample into m_{625} magnitude ranges from 15 to 30 with intervals of 0.5, and fitting them into Eq. (3) for each bin. This functional form assigns a low probability weight to bright galaxies at high redshifts.

Constructing priors based on the true redshifts in EL-COSMOS is a reasonable choice, as it minimizes the risk of adopting inappropriate priors: the reference catalog (COSMOS2015) is both deeper and more complete than our target survey 7DS (Laigle et al. 2016; Hoyle et al. 2018). Note that propagated uncertainties in these priors—arising from Poisson sampling errors (shot noise) and/or sample variances due to large-scale structures—are expected to append further uncertainties at the 1% level for $z < 1.5$. However, theoretical approaches to mitigate these effects already exist (e.g., Sánchez et al. 2020). Given the reliability of our reference data, we suppose the additional uncertainties from our customized priors are ignorable.

In practical applications, priors are expected to be constructed from a large spectroscopic (e.g., DESI Collaboration et al. 2016) and complementary photometric samples (e.g., Weaver et al. 2022; Duncan 2022) that offer high completeness at $z \lesssim 1$. Looking ahead, upcoming datasets such as LSST (Graham et al. 2018) and Euclid (Euclid Collaboration et al. 2020) will also serve as prospective resources for building reliable priors at higher redshifts.

For characterizing the accuracy of photometric redshifts, we introduce three metrics: *Catastrophic failure* η, *NMAD* $\sigma_{\rm NMAD}$, and *Bias* b.

- *Catastrophic failure*, η, is the fraction of severely deviated photometric redshifts from spectroscopic redshifts more than 15%:

$$\eta = \mathrm{fraction}(|\mathrm{z_{spec}} - \mathrm{z_{phot}}|/(1 + \mathrm{z_{spec}}) > 0.15).$$

- *NMAD* (Normalized Median Absolute Deviation), $\sigma_{\rm NMAD}$, represents the 1σ uncertainty of photometric redshifts in a given spectroscopic redshift range:

$$\sigma_{\rm NMAD} = 1.48{\times}\mathrm{median}(|\Delta\mathrm{z}{-}\mathrm{median}(\Delta\mathrm{z})|/(1{+}\mathrm{z_{spec}})),$$

where $\Delta z = z_{\rm spec} - z_{\rm phot}$.

- *Bias*, b, measures the mean systematic offset of photometric redshifts versus spectroscopic redshifts of the sample:

$$b = \langle (z_{\rm phot} - z_{\rm spec})/(1 + z_{\rm spec}) \rangle \,,$$

where $\langle\cdot\rangle$ denotes the sample average.

4. 7DS PHOTOMETRIC REDSHIFT PERFORMANCE PREDICTION

In Figure 3, the photo-zs for 5 years of 7DS survey under different exposure times and prior conditions are displayed. The impact of increasing exposure time and the number of medium-band filters on photo-zs is explored.

4.1. *Photo-z Performance of Each 7DS Survey*

The IMS Y5 survey (the first row of Figure 3) provides highly accurate photo-zs with $\sigma_{\rm NMAD}$ of about 0.2 to 0.3% at $m_{625} < 22$. The photo-z accuracy deteriorates a bit at a fainter magnitude bin of $22 \leq m_{625} < 23$, but the survey still provides photo-z accuracy of 0.5% in $\sigma_{\rm NMAD}$. The catastrophic failure and bias is small as well with $\eta < 2.3\%$ and $b < 0.04$ at $m_{625} < 22$, and $\eta = 8.9\%$ and $b = -0.085$ at $22 \leq m_{625} < 23$.

The WTS Y5 survey's performance (from the second to fourth rows of Figure 3) is also excellent at brighter magnitudes with $\sigma_{\rm NMAD} = 0.002$ to 0.004 at $m_{625} < 21$ with inclusion of prior improving the photo-z accuracy. For the same magnitude bin, $b = 0.0$ to 0.004, and η is nearly 0% to a few % at most. The photo-z accuracy worsens at fainter magnitudes (up to $m_{625} \sim 22$), but is kept at a respectable level of less than a few per cent. But at the faintest magnitudes, both b and η become much worse, especially without prior.

The RIS survey (the last row of Figure 3) is the shallowest, so the performance of this survey should be considered only seriously at $m_{625} < 21$. At $19 \leq m_{625} < 20$, which is close to the survey depth, the photo-z accuracy is found to be $\sigma_{\rm NMAD} \sim 0.009$, and $\sigma \sim 0.054$ even at $20 \leq m_{625} < 21$. The bias and catastrophic failures are a problem ($\eta > 10\%$), but an application of a prior should significantly improve these metrics. A more detailed discussion of the impact of priors is elaborated in Section 4.4.

Overall, our results indicate that photo-z from 7DS can have accuracy better than 1% and a few tenths % for brighter sources and out to $z \sim 1$. This level of photo-z performance should allow us to trace large-scale structures of the universe at $z < 1$ and possibly beyond. The implications of these predicted metrics for scientific applications are further discussed in Section 4.5.

4.2. *Catastrophic Failures and Survey Depth*

We investigate the impact of survey depths on η by comparing the WTS Y5 with RIS and IMS Y5. This comparison allows us to probe the budget of how the S/N of 7DS influences the detection of spectral features and corresponding photo-zs. Overall, increasing the exposure time dramatically reduces the catastrophic failures. This effect is most prominent at a magnitude close to the survey depth. For example, at $21 \leq m_{625} < 22$, photo-zs from RIS with an exposure time of 600 seconds take up 52% of η, while those from IMS Y5 with 156,000 seconds contribute only 2.3%. This trend persists even at the fainter magnitude range $22 \leq m_{625} < 23$.

For WTS Y5, most of the failure photo-zs at $22 \leq m_{625} < 23$ correspond to galaxies fainter than the limiting magnitude at lower true redshifts $0 < z < 0.5$. Due to the insufficient S/N for the given exposure time, these galaxies are incorrectly identified as fainter galaxies at higher redshifts. However, for IMS Y5 with 10 times higher exposure time, the failed population is largely recovered (η from 31.6% to 8.9%). Similarly, $\sigma_{\rm NMAD}$ also decreases proportionally with η across all magnitude bins as exposure time increases.

4.3. *Effect of the Number of Medium-Band Filters*

To understand the impact of spectral resolution on photo-zs, we examine the role of medium-band filter configuration. A unique feature of the 7DS is its overlapping filters (i.e. $m_{400}, m_{413}, \ldots, m_{875}, m_{888}$), aiming at the increase in spectral resolution without compromising the S/N compared to the non-overlapping case (i.e. $m_{400}, m_{425}, \ldots, m_{850}, m_{875}$). We choose only 20 bands whose filter widths are not overlapping and compare the resulting photo-z with an overlapping 40 band system (the second and third row of Figure 3). Compared to WTS Y5 photo-zs results using only 20 bands that are not overlapping, the three metrics— η, $\sigma_{\rm NMAD}$, and b— exhibit better performance for the entire magnitude bins

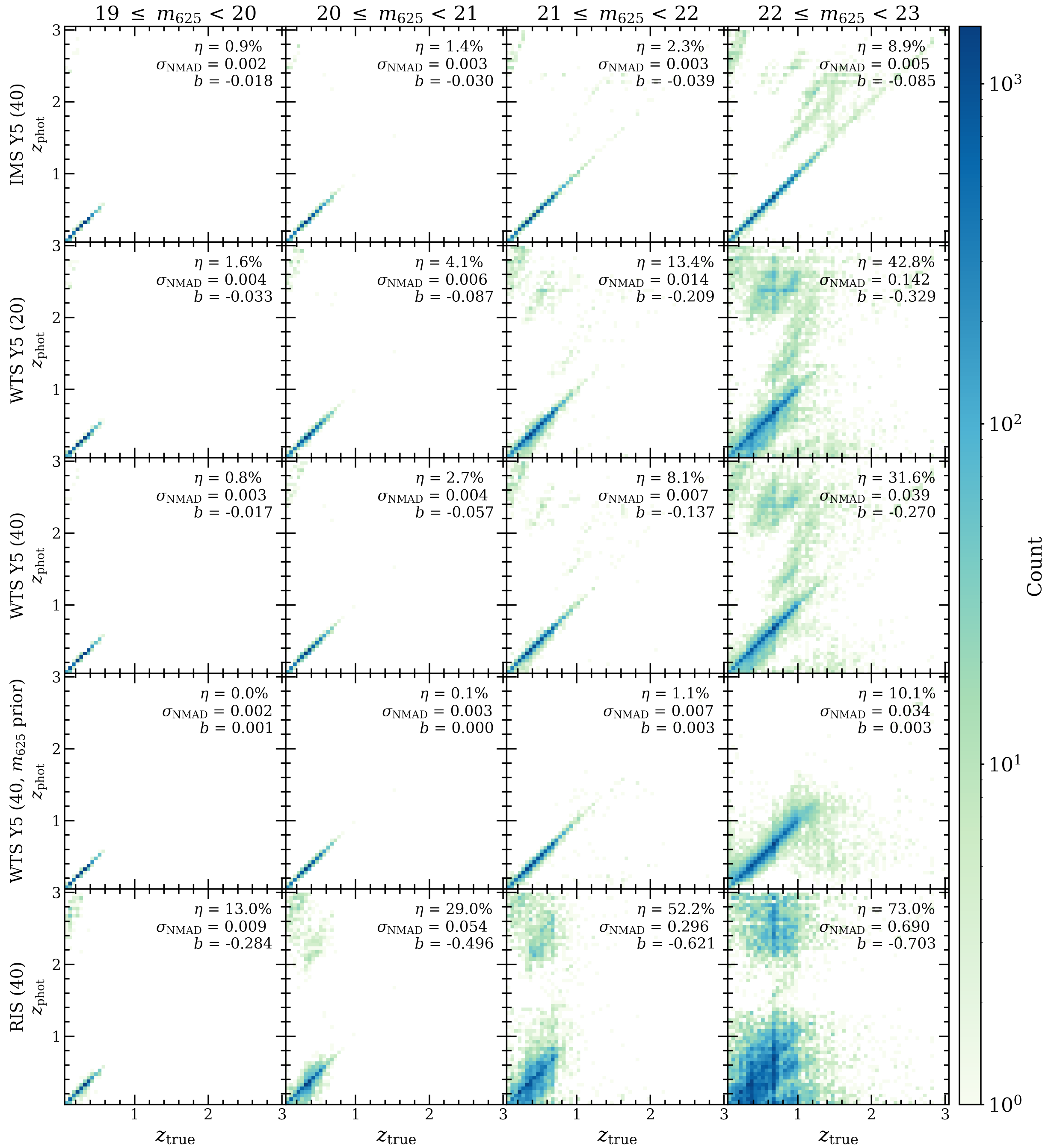

Figure 3. Comparisons between true redshifts $z_{\rm true}$ and predicted photometric redshifts $z_{\rm phot}$ from the 7DS mock catalog under different input conditions (from top to bottom: template fitted photometric redshifts from IMS Y5 40 bands, WTS Y5 20 bands, WTS Y5 40 bands, WTS Y5 40 bands with a m_{625} prior, and RIS 20 bands.)

in the 40-band system. This improvement can be seen for both bright and faint samples, highlighting the effectiveness of overlapping filter sets in boosting spectral resolution. The overlapping filters not only compensate for the relatively low S/N associated with the medium-band FWHM but also provide densely sampled photometric data points. The higher spectral resolution achieved at longer wavelengths for a given FWHM further aids in the accurate recovery of photo-zs for faint, high-redshift sources within the 7DS medium-band system.

We note that the regions where photo-zs deviate from true redshifts largely overlap between the results obtained from the 20- and 40-band systems. While some failure samples are recovered by significantly increasing the exposure time, as in the IMS Y5 results, uncertainties in determining photo-zs still remain. This is partly because degenerate color spaces between low and high redshifts intrinsically continue to hamper correct SED matching (Wolf et al. 2003; Cardamone et al. 2010). We will discuss the capability of the 7DS to capture key spectral features and resolve such degeneracies in more detail in Section 6.

4.4. *Magnitude Prior*

The most remarkable improvement after applying the prior (the fourth row of Figure 3) is the correction of falsely derived high photo-zs ($z_{\rm phot} > 2$) and low true redshifts ($z_{\rm true} < 1$). The prior breaks the degeneracies between low and high redshifts, showing a consistent trend of converging bias toward zero. However, by design, imposing the prior information is biased toward the lower photo-zs. For instance, new failure samples appear at $1.2 < z_{\rm true} < 2$ and $z_{\rm phot} < 1$. We suppose that this bias partly arises because this redshift range complies with the longest wavelength coverage of 7DS 888 nm in 7DS. Despite this potential problem, the prior should help minimize η for brighter galaxies, among which galaxies with $z_{\rm true} > 1.2$ are rare. Inclusion of longer wavelength data from other surveys should help reduce the bias, which will be examined in Section 5 and Section 6.2.

4.5. *Comparison with Previous Medium-Band Surveys*

We briefly discuss the face-value comparison between the predicted results from 7DS photo-zs and other medium-band surveys. Note that the criteria for photo-z metrics—such as catastrophic failure η (or outlier fraction), the photo-z calculation code, and wavelength coverage—may differ across surveys. Our prediction reveals a similar or lower $\sigma_{\rm NMAD}$ when compared to previous optical medium-band studies such as COMBO-17 (Wolf et al. 2003, $\sigma_{\rm NMAD} \approx 0.03$ at $m_R < 24$) and MUSYC (Cardamone et al. 2010, $\sigma_{\rm NMAD} = 0.008$ at $22 < m_R < 23$). On the contrary, our photo-z results indicate higher $\sigma_{\rm NMAD}$ and lower η than those from narrow-band studies like MiniJPAS (Hernán-Caballero et al. 2021, $\sigma_{\rm NMAD} < 0.003$ at $m_R < 23$ and *odds* > 0.82, $\eta = 0.39$ without any constraints) and PAU (Navarro-Gironés et al. 2023, see Figure 14). This trend can be explained by the differences in spectral resolution of these different surveys.

We briefly highlight the scientific applications of our predictions based on the requirements established in the literature. For galaxy evolution studies, the performance metrics achieved with IMS are highly competitive. For reference, Bordoloi et al. (2010) and Hildebrandt et al. (2017) suggest that reliable analyses require a minimum scatter of photo-z as $\sigma_{\rm NMAD} < 0.05$, while more ambitious surveys such as LSST adopt more stringent thresholds of $\sigma_{\rm NMAD} \sim 0.01$–$0.03$ (Ivezić et al. 2019). Because luminosity and stellar mass functions are only moderately sensitive to photo-z errors, our 7DS prediction of $\sigma_{\rm NMAD} \leq 0.01$ from IMS represents a clear advantage. In contrast, studies of galaxy environments demand substantially tighter precision: smearing along the line of sight due to photo-z errors can strongly bias the construction of the density field, further underscoring the value of our results.

As for cosmology, the requirements are considerably more stringent. Precision weak-lensing and large-scale structure measurements rely on minimizing both scatter and systematic bias in redshifts. For example, cosmic shear analyses demand photo-z biases at the level of $b \lesssim 0.002$, with η kept to a minimum (Knox et al. 2006; Hearin et al. 2010). The LSST requirements specify $b < 0.001$ for weak lensing and clustering over its 10-year baseline, together with a scatter of $\sigma_{\rm NMAD} < 0.003$ (Ivezić et al. 2019). The accuracy predicted for WTS therefore places it within reach of the most demanding cosmological applications.

To sum up, the 7DS surveys occupy a distinctive niche in multi-band surveys between broad- to narrow-band systems. The three surveys, IMS, WTS, and RIS, cover complementary regimes in area and depth, while sharing a consistent medium-band FWHM. Altogether, they form a unified framework that bridges wide, shallow surveys and narrow, deep experiments, thereby maximizing the scientific return of photo-z science across galaxy evolution and cosmology.

5. SYNERGY WITH OTHER SURVEYS

When combined with other surveys that offer higher S/N and different wavelength coverage, 7DS photo-zs can be further improved. In Figure 4, we present our findings after integrating data from other surveys (PS1, VIKING, and SPHEREx) with the 7DS dataset. For the 7DS WTS Y5, we adopt the case with 40 bands and no prior application.

5.1. *WTS Y5 + PAN-STAARS1*

By adding PS1 to 7DS (the first row of Figure 4), the resulting photo-z metrics improve slightly for samples at $m_{625} < 22$ but by a factor of ~ 2 for the faintest sample at $m_{625} > 22$ mag, where PS1 presumably complements for the relatively lower S/N of 7DS. While samples fainter than 7DS limiting magnitude benefit most from the high S/N broad-band surveys, it is important to note that the location of catastrophic failure samples

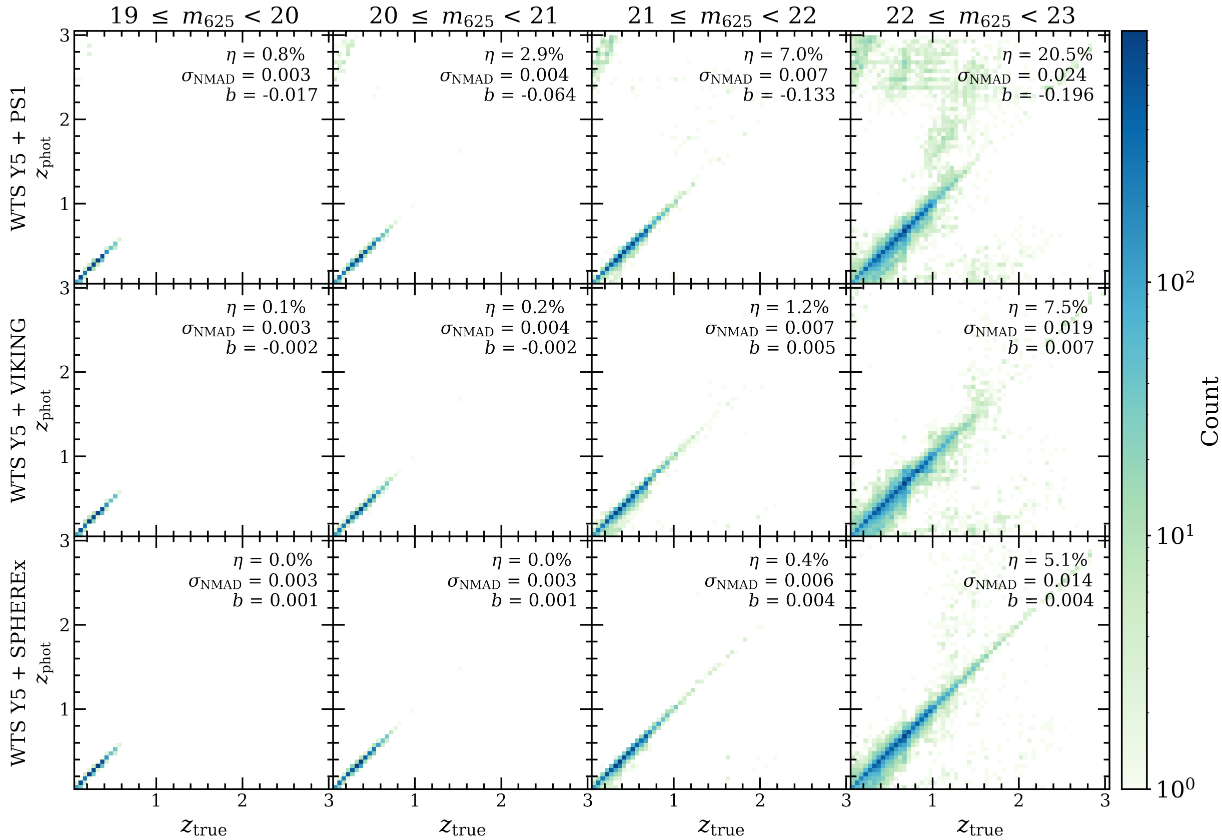

Figure 4. Comparisons between true redshifts and predicted photometric redshifts from the 7DS mock catalog with the combination of other surveys. From top to bottom: photometric redshifts from WTS Y5 + Pan-STARRS1, WTS Y5 + VIKING, and WTS Y5 + SPHEREx all-sky.

Table 2. Prediction results of photometric redshifts in 7DS and addition of other surveys

Surveys	$19 \le m_{625} < 20$	$20 \le m_{625} < 21$	$21 \le m_{625} < 22$	$22 \le m_{625} < 23$
WTS Y5 (20)	$(1.6\%, 0.004, -0.033)$	$(4.1\%, 0.006, -0.087)$	$(13.4\%, 0.014, -0.209)$	$(42.8\%, 0.142, -0.329)$
WTS Y5 (40)	$(0.8\%, 0.003, -0.017)$	$(2.7\%, 0.004, -0.057)$	$(8.1\%, 0.007, -0.137)$	$(31.6\%, 0.039, -0.270)$
WTS Y5 (m_{625} prior)	$(0.0\%, 0.002, 0.001)$	$(0.1\%, 0.003, -0.000)$	$(1.1\%, 0.007, 0.003)$	$(10.1\%, 0.034, 0.003)$
RIS Y5	$(13.0\%, 0.009, -0.284)$	$(29.0\%, 0.054, -0.496)$	$(52.2\%, 0.296, -0.621)$	$(73.0\%, 0.690, -0.703)$
IMS Y5	$(0.9\%, 0.002, -0.018)$	$(1.4\%, 0.003, -0.030)$	$(2.3\%, 0.003, -0.039)$	$(8.9\%, 0.005, -0.085)$
WTS Y5 + PS1	$(0.8\%, 0.003, -0.017)$	$(2.9\%, 0.004, -0.064)$	$(7.0\%, 0.007, -0.133)$	$(20.5\%, 0.024, -0.196)$
WTS Y5 + VIKING	$(0.1\%, 0.003, -0.002)$	$(0.2\%, 0.004, -0.002)$	$(1.2\%, 0.007, 0.005)$	$(7.5\%, 0.019, 0.007)$
WTS Y5 + SPHEREx	$(0.0\%, 0.003, 0.001)$	$(0.0\%, 0.003, 0.001)$	$(0.4\%, 0.006, 0.004)$	$(5.1\%, 0.014, 0.004)$

Note—(η, $\sigma_{\rm NMAD}$, b). We use 40 7DS band filters and template fitting only method except for applying prior (third row).

in the redshift space remains unchanged before and after adding PS1 (e.g., Graham et al. 2020). As discussed in Section 4.2, an increase in the S/N cannot eliminate the contamination caused by intrinsic spectral degeneracies. A more detailed analysis of this issue is presented in the context of SEDs in Section 6.1 (see also Figure 7 for a preview of the spectral resolution of 7DS and PS1).

Furthermore, we confirm that the addition of PS1 broad-bands can sometimes lead to deviations in photo-zs due to its high S/N. While 1,762 out of 20,654 samples brighter than the 5σ limiting magnitude $m_{625} \le 22.62$ benefit from the addition of PS1, 1,018 out of 20,654 samples, originally successful with WTS Y5 alone, show the opposite trend. This occurs because the χ^2 values from the template-fitting process are weighted by their errors, and a simplistic approach may result in inaccurate calculations. This finding is consistent with predictions by Benítez et al. (2009a) and Benitez et al. (2014), which suggests that a limited number of broad-band filters can be more prone to color-redshift degeneracies, and the photo-z derived may not benefit from higher S/N to the extent expected.

Nonetheless, there remains further scope for boosting the combination of medium-band datasets with high S/N broad-band data through more sophisticated approaches. For example, Hernán-Caballero et al. (2024) demonstrates the effectiveness of conflating the full redshift probability distribution function (zPDF) from narrow-band data (J-PAS) and broad-band data (HSC-SSP), rather than relying solely on single-point photo-z estimates. They point out two main challenges in deriving photo-zs from both broad- and narrow-band observations: (1) cross-calibration across different data-processing pipelines and instruments, which involves highly complicated systematics that must be controlled to produce homogeneous photometry, and (2) increased vulnerability of faint sources to color degeneracies in template fitting, whereas brighter counterparts are more robust in recovering their true redshifts among a large template set. Therefore, adopting careful strategies that catch the full probability distribution— encoding spectral features from narrow-band surveys while filtering out spurious peaks secured by high S/N broad-bands—can maximize their synergy (Kovač et al. 2010; Barro et al. 2019)

5.2. *WTS Y5 + VIKING*

The extra near-IR information from VIKING (the second row of Figure 4) leads to better photo-zs compared to WTS Y5 alone and WTS Y5 + PS1 across all magnitude bins. The inclusion of near-IR not only enhances the photo-z metrics but also helps recover some of the previously catastrophic failure samples. Specifically, the catastrophic failures, previously populating around low $z_{\rm true}$ and high $z_{\rm phot}$, are largely mitigated, significantly reducing the bias. This improvement from near-IR coverage differs from the effect of simply increasing S/N. We suppose that 8875 Å to 2.1 μm wavelength information in VIKING contributes to breaking up the color degeneracies up to redshifts $z = 2$ to 3. Consequently, the clump of points at $z_{\rm phot} > 2$ and $z_{\rm true} < 1$ is accurately aligned with its true redshift (see the upcoming Section 6.2 for the physical origin of the color degeneracy and Figure 8 as an example of SEDs from 7DS and near-IR surveys). This advantage of incorporating near-IR is consistent with previous works (e.g., Benítez et al. 2009a; Benitez et al. 2014).

5.3. *WTS Y5 + SPHEREx*

A significant synergy is observed with the combination of 7DS and SPHEREx (the third row of Figure 4). SPHEREx extends its wavelength coverage up to 5 μm, with 96 LVFs in this study. At $19 \leq m_{625} < 22$, $\sigma_{\rm NMAD}$ remains sub-percent accuracy, so does b and η. Even in the fainter magnitude bin $22 \leq m_{625} < 23$, only 2.5% of samples are classified as catastrophic failures while the photo-z accuracy remains high. It is also notable that the scatter between $z_{\rm phot}$ and $z_{\rm true}$ is reduced more than in any other combinations probed in our work.

This improvement further exemplifies the critical role of medium-band filters as a key hunter for spectral features, especially in combination with IR surveys. Previous forecasting studies have already emphasized the mutual benefits of integrating IR and optical broad-band data for photo-z performance (e.g., Doré et al. 2016; Stickley et al. 2016; Rhodes et al. 2017; Doré et al. 2018; Graham et al. 2020). For instance, Doré et al. (2018) demonstrates that augmenting SPHEREx-shallow with Euclid data can reduce the $\sigma_{\rm NMAD}$ of bright samples at $18 < RIZ < 19$ from 0.013 to 0.005, and for fainter sources near the Euclid magnitude limit ($23.5 < RIZ < 24$) with SPHEREx-deep from 0.054 to 0.015. Similarly, combining LSST and Euclid decreases the standard deviation of photo-z by 20% at $z < 1$ and lowers the outlier fractions by 40% (Graham et al. 2020). Within this context, our results provide strong quantitative evidence that medium-band + IR survey synergies can deliver substantial improvements in redshift accuracy, establishing 7DS as a powerful partner for SPHEREx and future space-based IR missions.

The overall photo-z prediction results in Section 5 are illustrated in Figure 5 and summarized in Table 2.

6. DISCUSSION

As a complementary analysis to the previous statistical approach, we look into individual SEDs and evaluate how higher S/N and extra information improve the photo-z metrics in Section 6.1 and Section 6.2. Additionally, we assess the detectability of emission lines from 7DS in Section 6.3. *This is the high spot of our study, which shows the power of 7DS's medium-band filter sets.*

6.1. *Broad Band with High S/N vs. Medium Band with High R*

Here, we compare the impact of S/N and spectral resolution on the photo-z accuracy. Figure 6 presents a detailed comparison of photo-zs obtained from PS1 and 7DS without applying any priors. Overall, η for photo-zs derived using the template-fitting method in WTS Y5 increases as sample magnitudes increase, whereas in PS1, η remains in a similar range across magnitudes. Despite the deeper 5σ depth (23.2) of PS1's r-band compared to $m_{625} = 22.62$ in WTS Y5, photo-zs from PS1

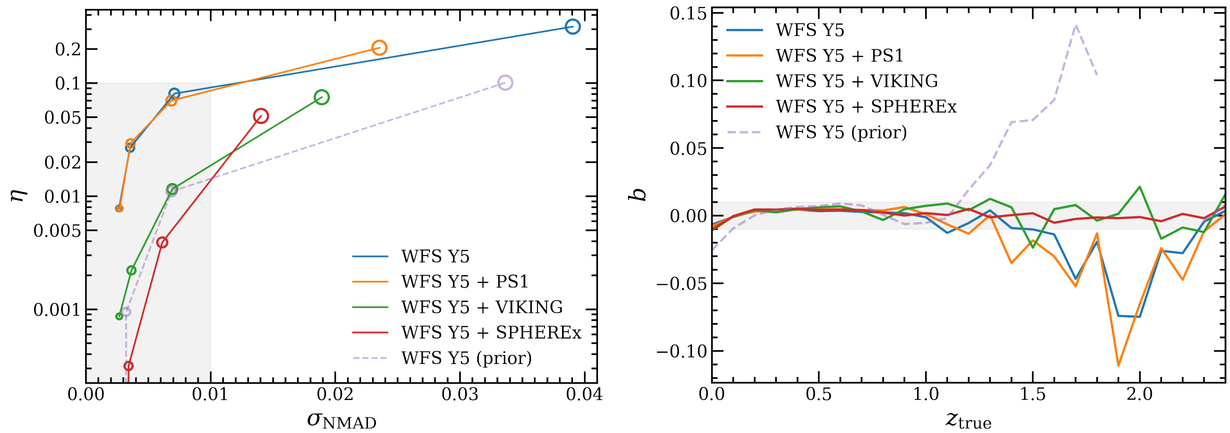

Figure 5. Overall photo-z metrics for WTS Y5 and combination with other surveys. Left panel: catastrophic failure η as a function of NMAD $\sigma_{\rm NMAD}$. The size of markers represents the magnitude range (19, 20, 21, 22) in increasing order. Right panel: Bias b as a function of true redshift. The area smaller than the bench marking values, $\sigma_{\rm NMAD} = 0.01$, $\eta = 0.10$, and $b = 0.01$, were shaded in gray.

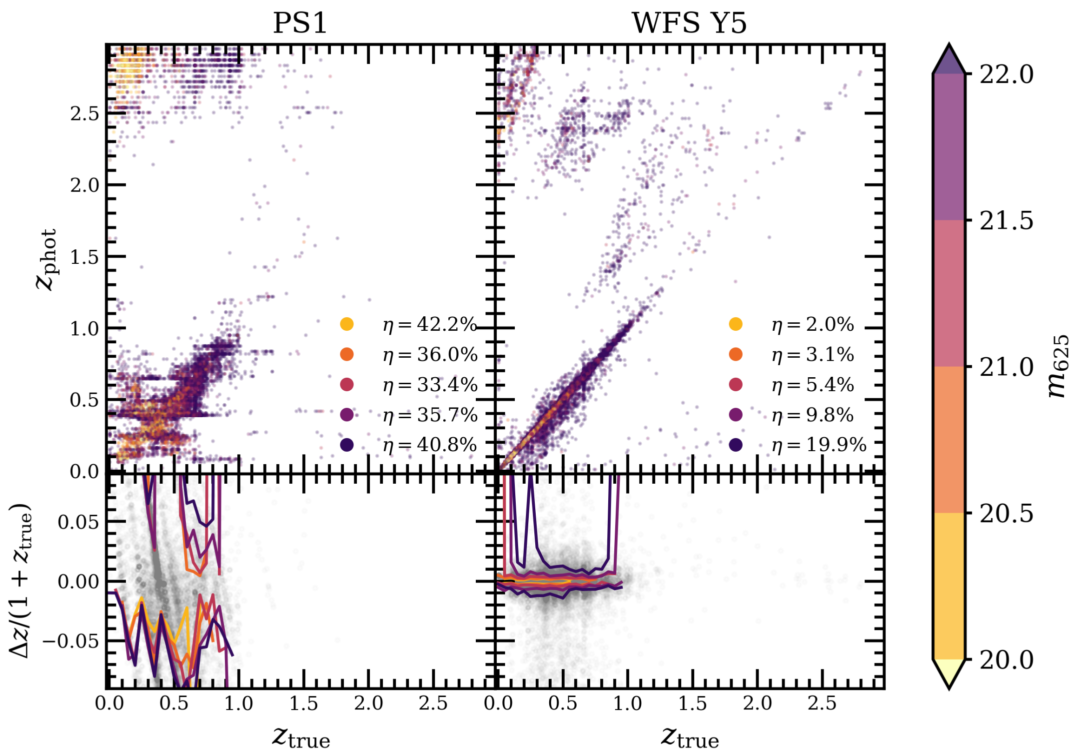

Figure 6. A comparison of photo-zs obtained from PS1 and 7DS for a given magnitude bin at $20 \leq m_{625} \leq 22$. No priors are applied for both results.

can deviate from their true redshifts even for bright samples ($m_r < 20$). This is because photo-zs from PS1 broad-bands with template fitting methods are more susceptible to color degeneracy, resulting in increased contamination. In contrast, for 7DS, most misclassified galaxies are relatively faint, with magnitudes comparable to or fainter than the limiting magnitude. Consistently, as noted in Section 5.1, merely increasing S/N does not proportionally improve photo-z accuracy and cannot recover all catastrophic failures. Instead, more detailed spectral diagnostics or additional wavelength information are needed to accurately resolve their features.

Figure 7 illustrates the comparison of matched SEDs from WTS Y5 and PS1 for a quiescent and a star-forming galaxy. For the quiescent galaxy with a true

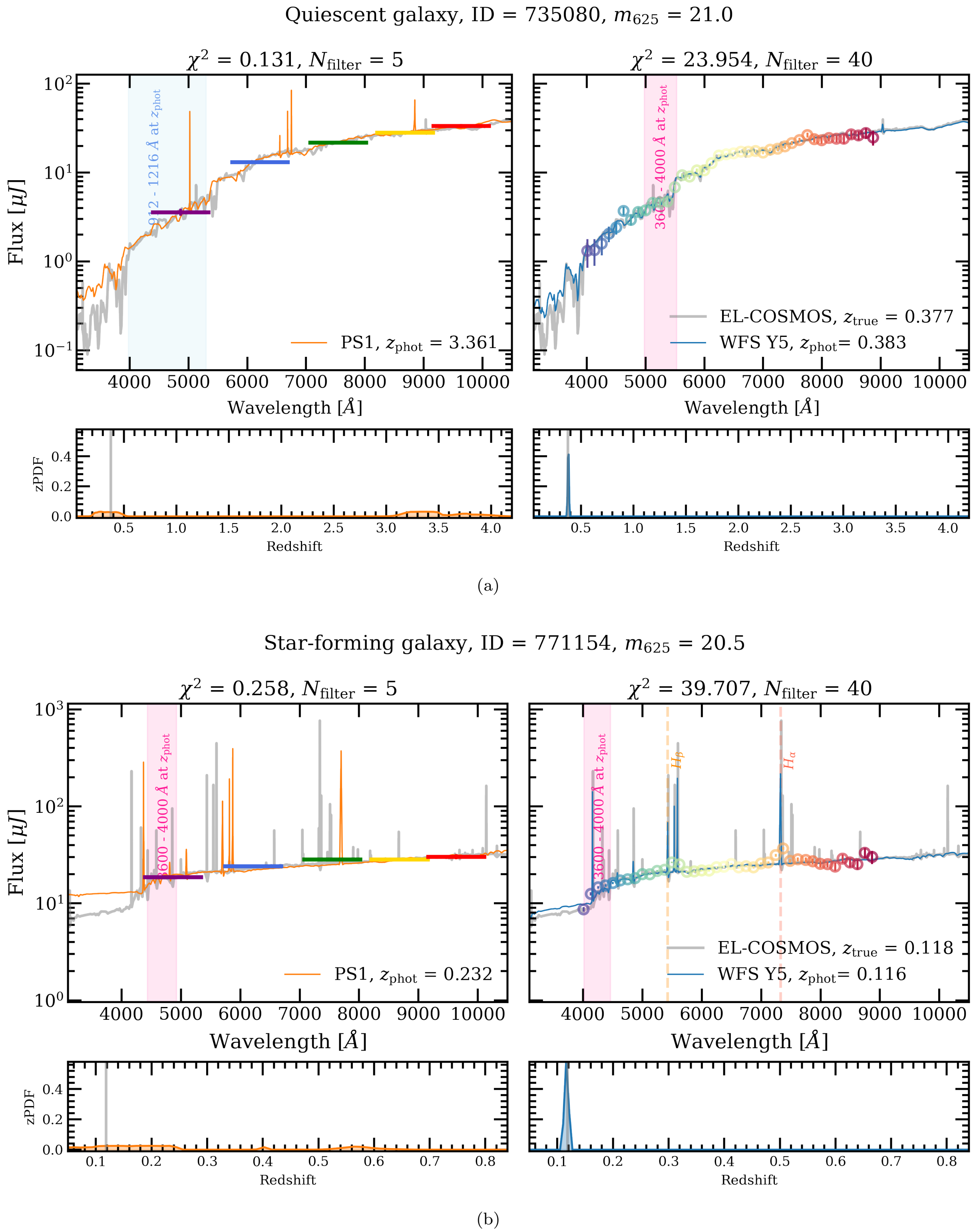

Figure 7. Examples of matched SEDs and zPDF from 7DS and PS1. (a) A quiescent galaxy at $z_{\rm true} = 0.377$ with a Balmer break. (b) A star-forming galaxy at $z_{\rm true} = 0.118$ with emission lines. The original SED from EL-COSMOS is shown as a gray line. The orange line is the best-fit photo-z from PS1 and the blue line from WTS Y5.

redshift of $z_{\rm true} = 0.377$, the original SED from EL-COSMOS clearly shows the Balmer and 4000 Å breaks

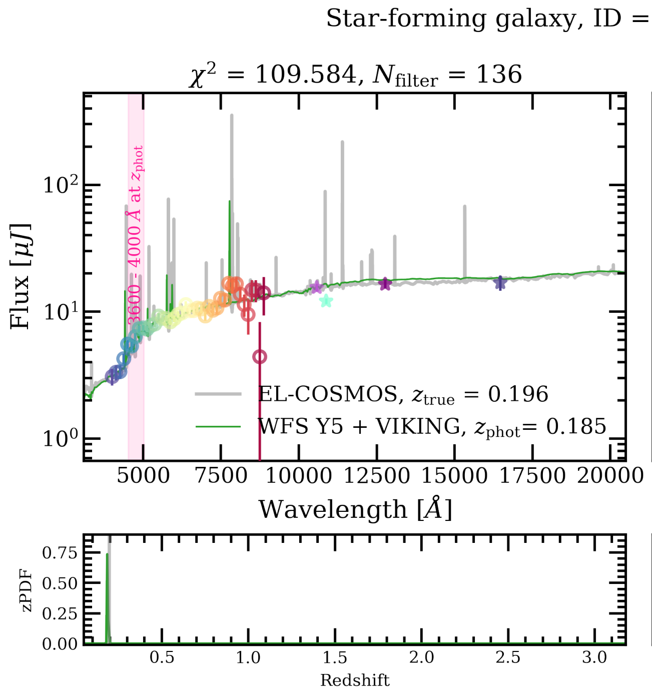

(a)

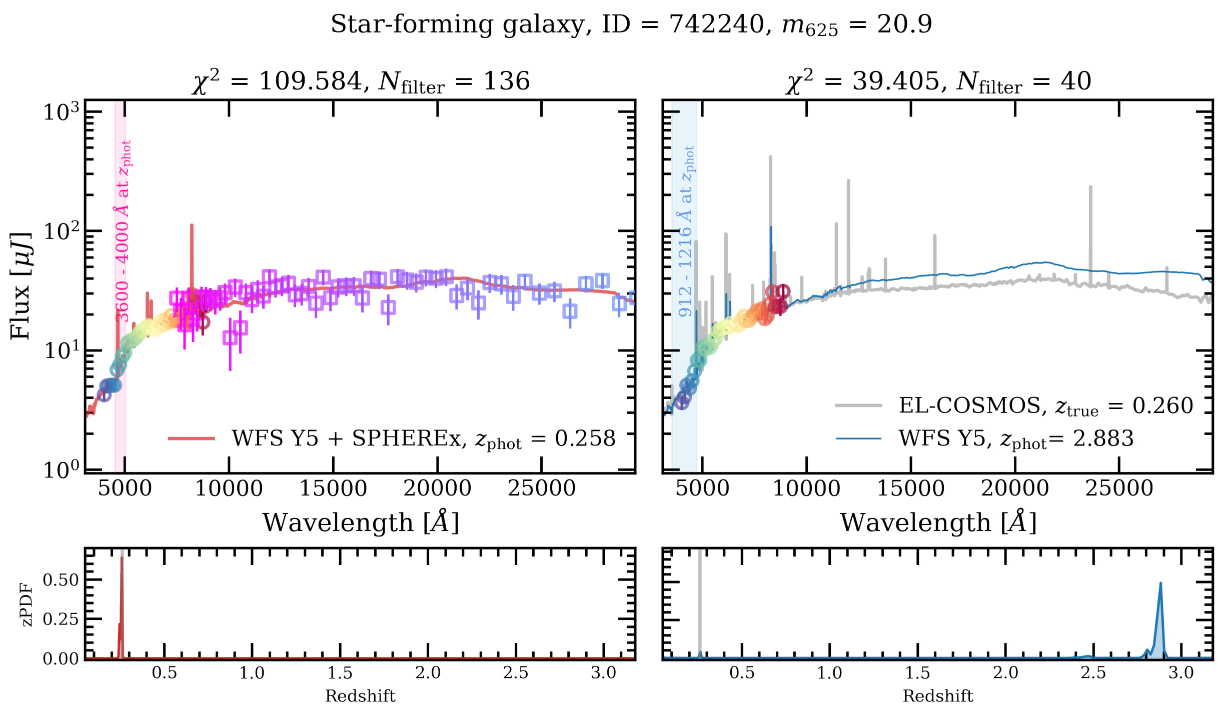

(b)

Figure 8. Examples of matched SEDs and zPDF from 7DS alone and in combination with (a) VIKING and (b) SPHEREx.

near the observed wavelength 5000–5500 Å. However, the matched SED from PS1 misinterprets this feature as a Lyman break for a galaxy at a higher redshift $z_{\rm phot}$ = 3.361. The relatively low spectral resolution of broad-band filters in PS1 fails to distinguish these detailed spectral features, resulting in a much higher photo-z. On the other hand, the photometric dataset from WTS Y5 captures the features before and after the breaks. The zPDF for the PS1 data shows significant ambiguity, with a broad spread between $0 < z_{\rm phot} < 0.5$ and $3.0 < z_{\rm phot} < 3.5$. In comparison, the zPDF from 7DS is sharply concentrated around the true redshift. This demonstrates that photo-z accuracy benefits highly from densely sampled photo-spectra, which reduces the ambiguity in identifying spectral break features across different redshifts. Lifting such degeneracy is particularly advantageous for quiescent galaxies at low redshift, whose break features are more pronounced than for star-forming galaxies (Stabenau et al. 2008; Girelli et al. 2019).

Emission lines from star-forming galaxies are another crucial factor in determining the SEDs. The corresponding example shown in the lower panel of Figure 7 illustrates this point. For PS1, while the continuum of the matched SED generally overlaps with the true SED, their emission lines do not. The coarse sampling of the data misses the detailed features of the emission lines, obscuring the accurate photo-z calculation. On the contrary, the SED from 7DS captures strong emission lines such as H_α and H_β of the true SED. The broad-band system in PS1 dilutes these features when used alone. This result again highlights the importance of spectral resolution in probing spectral features and unscrambling the potential color degeneracies inherent in SEDs.

At last, from the perspective of zPDF, we revisit the possibility of improving the photo-z estimate. As noted in Figure 7, the zPDF derived from PS1, which yields an incorrect photo-z, spans much broader redshift space than the case from 7DS. This broader distribution makes point estimates such as `z_a` and/or `z_m2` less representative of the true redshift, thereby degrading photo-z metrics that rely solely on them. Put differently, reducing the width of the zPDF and an effective strategy would directly lead to more reliable and less contaminated photo-z metrics (Carrasco Kind & Brunner 2013; D'Isanto & Polsterer 2018).

6.2. *Breaking Color Degeneracies with Addition of near-IR Data*

Along with the need for higher spectral resolution to derive accurate photo-zs, solely relying on optical wavelength information faces challenges in differentiating the similar spectral features at low and high redshifts. We analyze the impact of near-IR data on matched SEDs, covering from 8875 Å to 2.1 μm in VIKING and from 0.75 to 5.0 μm in SPHEREx, as illustrated in Figure 8. In the upper panel, the matched SED from 7DS alone diverges from the true SED in the near-IR region. Due to the poor S/N near 8875 Å and the absence of longer wavelength information, a low redshift galaxy at $z_{\rm true} = 0.196$ is misclassified as having a higher redshift at $z_{\rm phot} = 2.676$. However, by providing the VIKING's additional data points covering from 8875 Å to 2.1 μm, the SED matches the true SED accurately. A similar improvement is observed with SPHEREx, as shown in the lower panel. We attribute this to SPHEREx's denser and wider coverage from 0.75 μm to 5.0 μm, which enables one to sample redshifted 1.6 μm effectively.

6.3. *Tracing emission lines in 7DS medium-band filters*

Thanks to the 25 nm FWHM of 7DS medium-band filters, it is possible to detect strong emission lines indirectly. The emission line diagnostics provide fundamental constraints on galactic properties, linked to the ionized interstellar medium (Kewley et al. 2019). For example, from diagnostics such as electron density and ISM pressure, one can infer the ionization state, chemical abundance, and the dominant excitation sources of galaxies (e.g. Kewley et al. 2013; Peimbert et al. 2017). The use of photo-spectra for diagnosing emission features has been suggested (e.g. Laigle et al. 2019) and implemented in various studies (e.g. Griffiths et al. 2021; Iglesias-Páramo et al. 2022; Williams et al. 2023; Withers et al. 2023; Sarrouh et al. 2024). For example, Bonoli et al. (2021) demonstrated that narrow-band filters with a 145 Å width can detect emission lines from star-forming galaxies, thereby improving the accuracy of photo-z measurements. Moreover, Renard et al. (2022) also suggests the direct measurement of 4000 Å break using narrow-band filters, which allows for the reproduction of empirical relations such as D4000-SFR and D4000-mass relation in spectroscopy.

In this regard, we can experiment to check 7DS's potential for tracing emission lines by comparing the color excess between the broad-band and medium-band filters. An example of $m_r - m_{625}$ as a function of redshifts is shown in Figure 9. Interestingly, this comparison reveals that the color excess between broad- and medium-band filters corresponds to known emission lines and breaks. Specifically, redshifted emission lines (e.g. H_α, H_β, [OIII], and [OII]) coincide to lie at the positive $m_r - m_{625}$ color while spectral breaks (4000 Å and Balmer break) are associated with negative values. This alignment suggests that 7DS can effectively trace these important spectral features. Other examples of HSC g and i band color excess are described in Figure B.1 and Figure B.2.

We select galaxies exhibiting strong color excess and control samples to investigate the relationship between the strength of this excess and the potential to catch

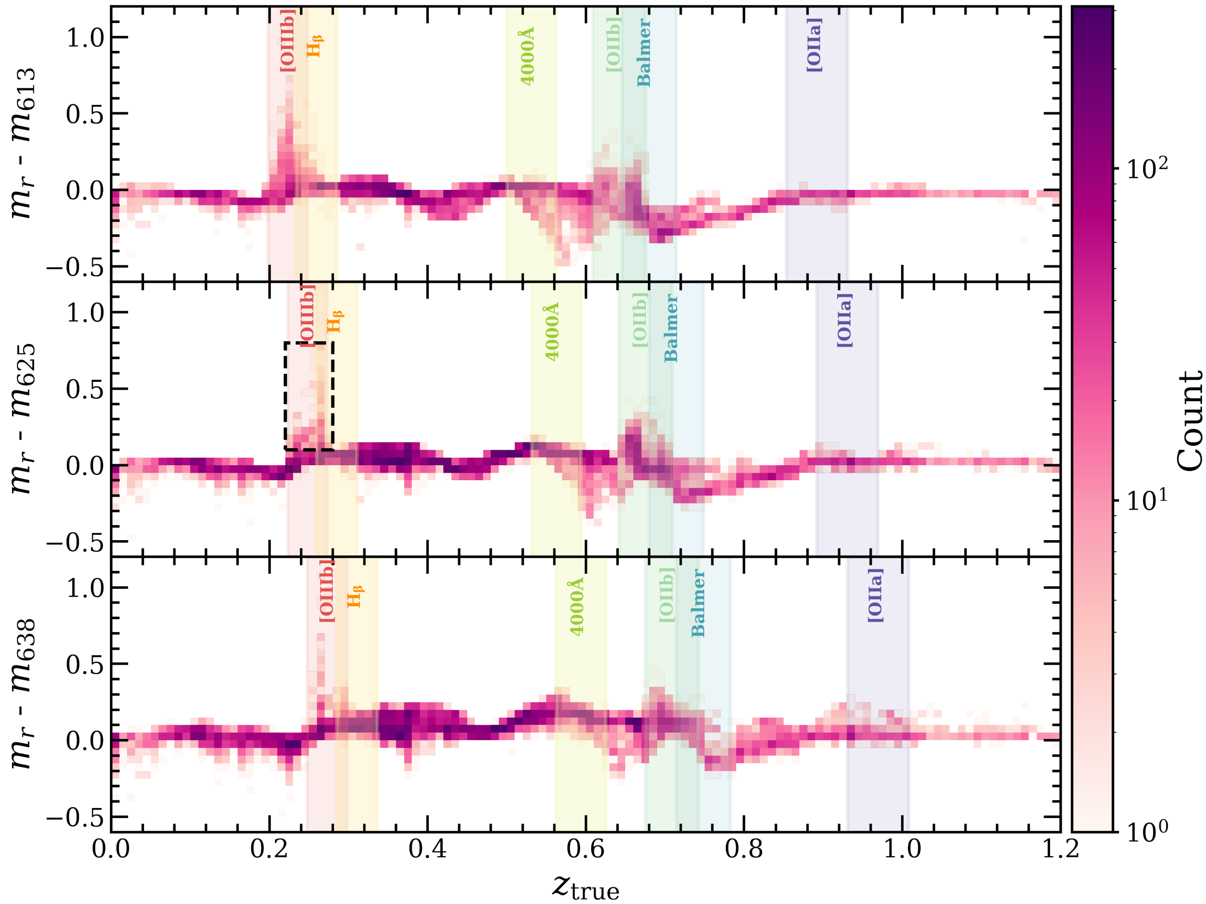

Figure 9. A $m_r - m_{625}$ color as a function of true redshifts (middle panel). Adjacent colors of m_{613} (top panel) and m_{638} (bottom panel) are also described.

spectral features for photo-z calculations. We focus on sample galaxies at $0.2 < z_{\rm true} < 0.3$ and $m_r - m_{625} > 0.2$ with S/N > 10 at m_{625} (highlighted in the dashed box in the second row of Figure 9) as potential strong emission line candidates. We compare these candidates with residual samples that meet the same S/N criteria but do not show a significant color excess ($0.2 < z_{\rm true} < 0.3$, $m_r - m_{625} < 0.2$, and S/N > 10 at m_{625}). The color excess threshold of 0.2 mag is set to correspond to a 5σ uncertainty at the limiting magnitude of m_{625}. In total, we identify 54 galaxies with $m_r - m_{625} > 0.2$ and 1,740 with $m_r - m_{625} < 0.2$. For more precise photo-z estimates, the ability to detect emission lines is also beneficial. While no catastrophic failure galaxies are found with color excess samples, 187 galaxies ($\sim 11\%$) without color excess deviate by more than 15% from their true redshifts.

We confirm a similar excess pattern when replacing the HSC broad-band with fluxes near the given filter. To summarize, 7DS photometric data can serve as a useful indicator of emission lines.

7. CONCLUSION

In this paper, we explore how reliably medium-band filters in the 7-Dimensional Sky Survey produce photometric redshifts. We use simulation data that accounts for observational systematics and survey plans to provide a comprehensive prediction of photometric redshifts in 7DS. Our findings indicate that further improvement is achievable when combined with other surveys, SPHEREx in particular. We conclude our findings below.

1. Using model SEDs from EL-COSMOS, we construct mock photometric data that resemble the 7DS setup. This includes accounting for telescope and detector efficiencies, as well as sky transmission at the observatory site in Chile. We produce a mock catalog containing half a million sources and derive photometric redshifts using the `EAZY` code, covering the 5-year Wide-field Time-Domain Survey (WTS Y5), Reference Imaging Survey (RIS), and 5-year Intensive Monitoring Survey (IMS Y5)

in 7DS, along with other surveys including Pan-STARRS1, VIKING, and SPHEREx all-sky.

2. Overall, the WTS Y5 observed with 40 medium-band filters achieves a catastrophic failure fraction η from 0.8 to 8.1%, NMAD $\sigma_{\rm NMAD}$ from 0.003 to 0.007, and bias b from -0.017 to -0.137 at $19 \leq m_{625} < 22$. The IMS Y5, whose on-source exposure time is 10 times longer than the WTS Y5, can significantly reduce catastrophic failures at faint magnitudes around the WTS Y5 limiting magnitudes. However, merely increasing exposure time does not fully resolve contamination issues. Instead, additional information, such as magnitude priors or near-IR coverage, is crucial for further improvements.

3. Combining 7DS with other surveys PS1, VIKING, and SPHEREx all-sky yields overall improvements of photo-zs. While PS1 helps recover true redshifts from samples with insufficient S/N, it does not entirely resolve the intrinsic color degeneracies between faint galaxies at low and high redshifts. The association with near-IR information from VIKING and SPHERE, however, plays a complementary role by covering the wavelengths not probed by 7DS.

4. We compare the matched SEDs of individual galaxies obtained from template fitting. The 7DS data effectively capture spectral features of 4000 Å and Balmer break for quiescent galaxies and emission lines for star-forming galaxies, despite having lower S/N than PS1. Furthermore, the optical-only 7DS data can obtain more constraining power in synergy with near-IR data from VIKING and SPHEREx. They provide the coverage of 8875 Å to 2.1 μm from VIKING and 0.75–5.0 μm from SPHEREx, respectively, as zPDF becomes sharper and concentrated around the true redshift.

5. We demonstrate the potential application of medium-band filters to trace strong emission lines. By analyzing the color excess between 7DS medium-band and adjacent PS1 broad-band photometric data, we identify features corresponding to spectral breaks and emission lines.

To conclude, 7DS offers promising prospects for accurate redshift measurements. The medium-band filters, with a spectral resolution of $R \sim 50$ of FWHM $= 25$ nm, play a crucial role in detecting spectral diagnostics that are otherwise missed. With the aid of additional data, particularly from SPHEREx, we expect to extend these capabilities further to enhance our understanding of astrophysics and cosmology.

This work was supported by the National Research Foundation of Korea (NRF) grant No. 2021M3F7A1084525, funded by the Korea government (MSIT). SL acknowledges support from the National Research Foundation of Korea (NRF) grant (RS-2025-00573214) funded by the Korea government(MSIT). J.H.K. acknowledges the support from the National Research Foundation of Korea (NRF) grants, No. 2021M3F7A1084525 and No. 2020R1A2C3011091, and the Institute of Information & Communications Technology Planning & Evaluation (IITP) grant, No. RS-2021-II212068 funded by the Korean government (MSIT).

We acknowledge the use of EL-COSMOS. This research has made use of the ASPIC database, operated at CeSAM/LAM, Marseille, France.

APPENDIX

A. 7DS DATA SPECIFICATION

Table A.1. Data Specifications of 7-Dimensional Telescope, detector, and atmospheric transmission

	Telescopes
Telescope	Planewave DR500
Number of telescopes	20
Aperture size	50.8 cm ($f/3$)
Effective focal length	1537.3 mm
Central Obscuration	29.8 cm
	Detector
Camera	Moravian Camera C3-61000PRO
Detector	IMX455 rolling shutter back-illuminated CMOS
Resolution	9576×6388
Pixel size	$3.76\ \mu m \times 3.76\ \mu m$
Dark current	$0.01\ -e/s$
Readout noise	$3\ -e$
	Model for Paranal site (VLT)
Airmass	1.3
PWV	2.5 mm

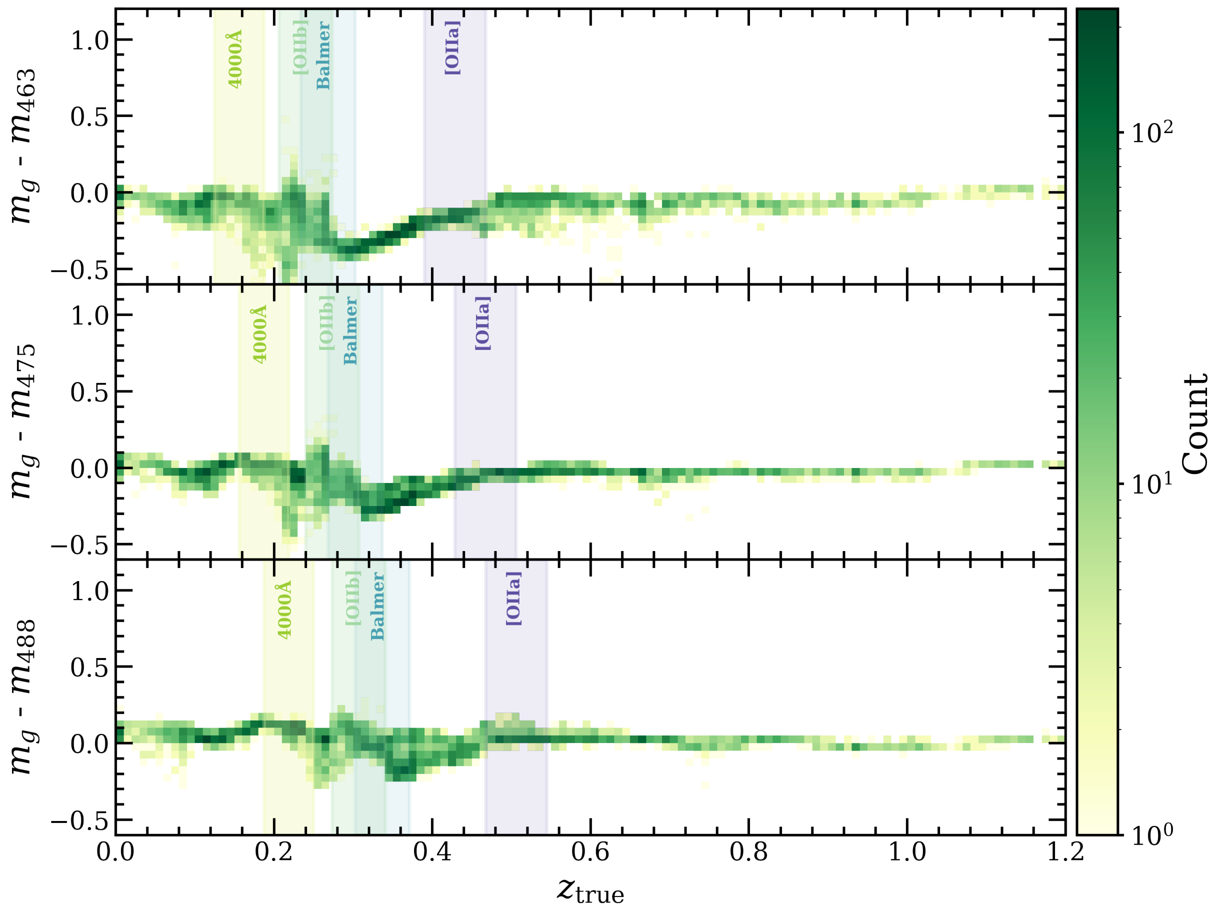

Figure B.1. Same as Figure 9 but for $m_g - m_{475}$ color.

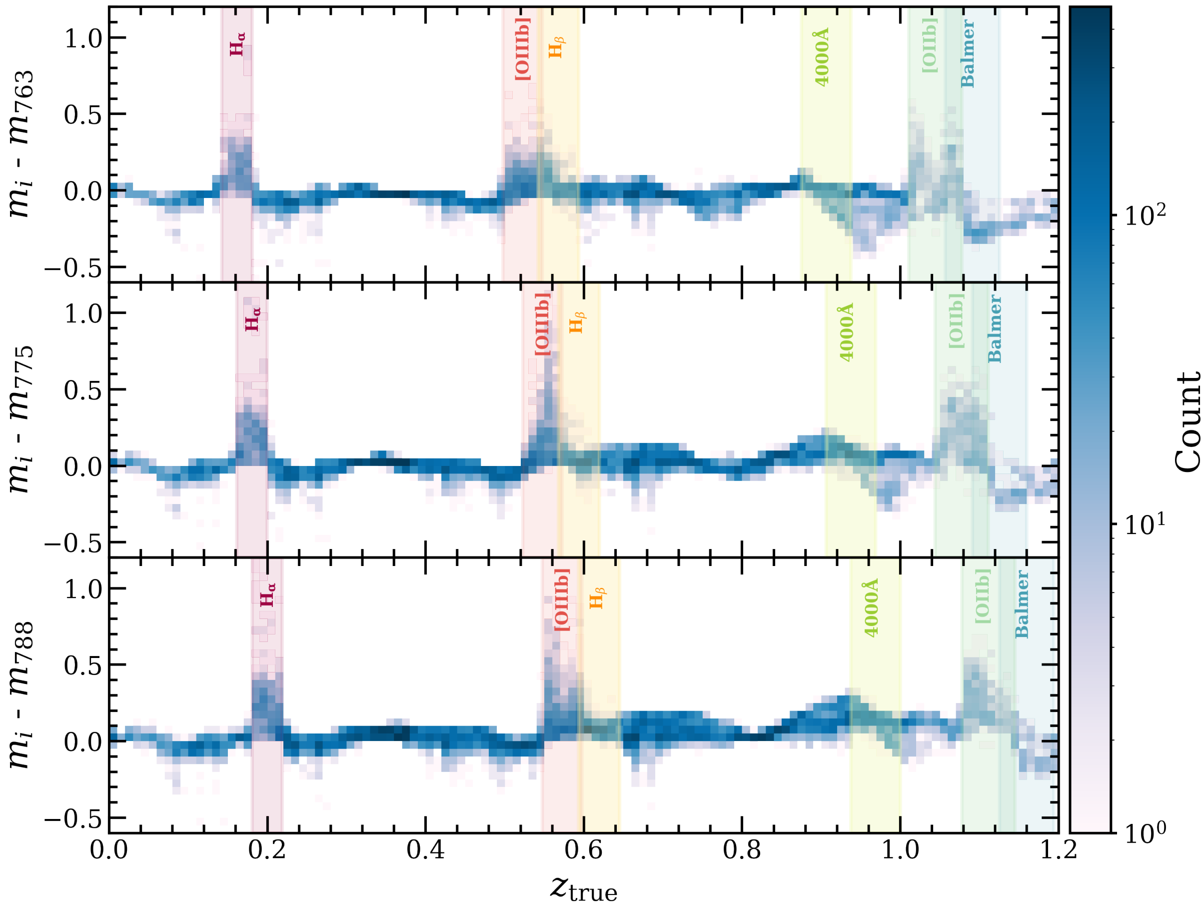

Figure B.2. Same as Figure 9 but for $m_i - m_{775}$ color.

REFERENCES

Abbott, B. P., Abbott, R., Abbott, T. D., et al. 2017, ApJL, 848, L12, doi: 10.3847/2041-8213/aa91c9

Abbott, T. M. C., Aguena, M., Allam, S., et al. 2022, PhRvD, 105, 043512, doi: 10.1103/PhysRevD.105.043512

Alarcon, A., Gaztanaga, E., Eriksen, M., et al. 2021, MNRAS, 501, 6103, doi: 10.1093/mnras/staa3659

Allen, C. W. 1976, Astrophysical Quantities

Allen, S. W., Evrard, A. E., & Mantz, A. B. 2011, ARA&A, 49, 409, doi: 10.1146/annurev-astro-081710-102514

Arnaboldi, M., Neeser, M. J., Parker, L. C., et al. 2007, The Messenger, 127, 28

Arnouts, S., Schiminovich, D., Ilbert, O., et al. 2005, ApJL, 619, L43, doi: 10.1086/426733

Barnett, R., Warren, S. J., Cross, N. J. G., et al. 2021, MNRAS, 501, 1663, doi: 10.1093/mnras/staa3808

Barro, G., Pérez-González, P. G., Cava, A., et al. 2019, ApJS, 243, 22, doi: 10.3847/1538-4365/ab23f2

Baum, W. A. 1962, in Problems of Extra-Galactic Research, ed. G. C. McVittie, Vol. 15, 390

Beltrame, M., Bonici, M., & Carbone, C. 2024, JCAP, 2024, 074, doi: 10.1088/1475-7516/2024/10/074

Benítez, N. 2000, ApJ, 536, 571, doi: 10.1086/308947

Benítez, N., Moles, M., Aguerri, J. A. L., et al. 2009a, ApJL, 692, L5, doi: 10.1088/0004-637X/692/1/L5

Benítez, N., Gaztañaga, E., Miquel, R., et al. 2009b, ApJ, 691, 241, doi: 10.1088/0004-637X/691/1/241

Benitez, N., Dupke, R., Moles, M., et al. 2014, arXiv e-prints, arXiv:1403.5237, doi: 10.48550/arXiv.1403.5237

Best, P. N., Ker, L. M., Simpson, C., Rigby, E. E., & Sabater, J. 2014, MNRAS, 445, 955, doi: 10.1093/mnras/stu1776

Blanton, M. R., & Roweis, S. 2007, AJ, 133, 734, doi: 10.1086/510127

Bolzonella, M., Miralles, J. M., & Pelló, R. 2000, A&A, 363, 476, doi: 10.48550/arXiv.astro-ph/0003380

Bonoli, S., Marín-Franch, A., Varela, J., et al. 2021, A&A, 653, A31, doi: 10.1051/0004-6361/202038841

Bordoloi, R., Lilly, S. J., & Amara, A. 2010, MNRAS, 406, 881, doi: 10.1111/j.1365-2966.2010.16765.x

Bouwens, R. J., Oesch, P. A., Stefanon, M., et al. 2021, AJ, 162, 47, doi: 10.3847/1538-3881/abf83e

Brammer, G. B., van Dokkum, P. G., & Coppi, P. 2008, ApJ, 686, 1503, doi: 10.1086/591786

Brammer, G. B., van Dokkum, P. G., Franx, M., et al. 2012, ApJS, 200, 13, doi: 10.1088/0067-0049/200/2/13

Bruzual, G., & Charlot, S. 2003, MNRAS, 344, 1000, doi: 10.1046/j.1365-8711.2003.06897.x

Burgarella, D., Buat, V., Gruppioni, C., et al. 2013, A&A, 554, A70, doi: 10.1051/0004-6361/201321651

Cardamone, C. N., van Dokkum, P. G., Urry, C. M., et al. 2010, ApJS, 189, 270, doi: 10.1088/0067-0049/189/2/270

Carrasco Kind, M., & Brunner, R. J. 2013, MNRAS, 432, 1483, doi: 10.1093/mnras/stt574

Cenarro, A. J., Moles, M., Cristóbal-Hornillos, D., et al. 2019, A&A, 622, A176, doi: 10.1051/0004-6361/201833036

Chabrier, G. 2003, PASP, 115, 763, doi: 10.1086/376392

Chambers, K. C., Magnier, E. A., Metcalfe, N., et al. 2016, arXiv e-prints, arXiv:1612.05560, doi: 10.48550/arXiv.1612.05560

Cheng, Y.-T., & Chang, T.-C. 2022, ApJ, 925, 136, doi: 10.3847/1538-4357/ac3aee

Cucciati, O., Tresse, L., Ilbert, O., et al. 2012, A&A, 539, A31, doi: 10.1051/0004-6361/201118010

Damen, M., Labbé, I., van Dokkum, P. G., et al. 2011, ApJ, 727, 1, doi: 10.1088/0004-637X/727/1/1

Davis, M., Faber, S. M., Newman, J., et al. 2003, in Society of Photo-Optical Instrumentation Engineers (SPIE) Conference Series, Vol. 4834, Discoveries and Research Prospects from 6- to 10-Meter-Class Telescopes II, ed. P. Guhathakurta, 161–172, doi: 10.1117/12.457897

DESI Collaboration, Aghamousa, A., Aguilar, J., et al. 2016, arXiv e-prints, arXiv:1611.00036, doi: 10.48550/arXiv.1611.00036

D'Isanto, A., & Polsterer, K. L. 2018, A&A, 609, A111, doi: 10.1051/0004-6361/201731326

Doré, O., Bock, J., Ashby, M., et al. 2014, arXiv e-prints, arXiv:1412.4872, doi: 10.48550/arXiv.1412.4872

Doré, O., Werner, M. W., Ashby, M., et al. 2016, arXiv e-prints, arXiv:1606.07039, doi: 10.48550/arXiv.1606.07039

Doré, O., Werner, M. W., Ashby, M. L. N., et al. 2018, arXiv e-prints, arXiv:1805.05489, doi: 10.48550/arXiv.1805.05489

Duncan, K. J. 2022, MNRAS, 512, 3662, doi: 10.1093/mnras/stac608

Edge, A., Sutherland, W., Kuijken, K., et al. 2013, The Messenger, 154, 32

Euclid Collaboration, Desprez, G., Paltani, S., et al. 2020, A&A, 644, A31, doi: 10.1051/0004-6361/202039403

Finkelstein, S. L., Papovich, C., Giavalisco, M., et al. 2010, ApJ, 719, 1250, doi: 10.1088/0004-637X/719/2/1250

Finkelstein, S. L., Ryan, Russell E., J., Papovich, C., et al. 2015, ApJ, 810, 71, doi: 10.1088/0004-637X/810/1/71

Fioc, M., & Rocca-Volmerange, B. 1997, A&A, 326, 950, doi: 10.48550/arXiv.astro-ph/9707017

Galametz, A., Saglia, R., Paltani, S., Apostolakos, N., & Dubath, P. 2017, A&A, 598, A20, doi: 10.1051/0004-6361/201629333

Girelli, G., Bolzonella, M., & Cimatti, A. 2019, A&A, 632, A80, doi: 10.1051/0004-6361/201834547

González Delgado, R. M., Díaz-García, L. A., de Amorim, A., et al. 2021, A&A, 649, A79, doi: 10.1051/0004-6361/202039849

Graham, M. L., Connolly, A. J., Ivezić, Ž., et al. 2018, AJ, 155, 1, doi: 10.3847/1538-3881/aa99d4

Graham, M. L., Connolly, A. J., Wang, W., et al. 2020, AJ, 159, 258, doi: 10.3847/1538-3881/ab8a43

Griffiths, A., Conselice, C. J., Ferreira, L., et al. 2021, MNRAS, 508, 3860, doi: 10.1093/mnras/stab2566

Hearin, A. P., Zentner, A. R., Ma, Z., & Huterer, D. 2010, ApJ, 720, 1351, doi: 10.1088/0004-637X/720/2/1351

Hernán-Caballero, A., Varela, J., López-Sanjuan, C., et al. 2021, A&A, 654, A101, doi: 10.1051/0004-6361/202141236

Hernán-Caballero, A., Akhlaghi, M., López-Sanjuan, C., et al. 2024, A&A, 684, A61, doi: 10.1051/0004-6361/202348513

Hildebrandt, H., Erben, T., Dietrich, J. P., et al. 2006, A&A, 452, 1121, doi: 10.1051/0004-6361:20054278

Hildebrandt, H., Viola, M., Heymans, C., et al. 2017, MNRAS, 465, 1454, doi: 10.1093/mnras/stw2805

Hoyle, B., Gruen, D., Bernstein, G. M., et al. 2018, MNRAS, 478, 592, doi: 10.1093/mnras/sty957

Iglesias-Páramo, J., Arroyo, A., Kehrig, C., et al. 2022, A&A, 665, A95, doi: 10.1051/0004-6361/202243931

Ilbert, O., Capak, P., Salvato, M., et al. 2009, ApJ, 690, 1236, doi: 10.1088/0004-637X/690/2/1236

Ilbert, O., Arnouts, S., Le Floc'h, E., et al. 2015, A&A, 579, A2, doi: 10.1051/0004-6361/201425176

Im, M. et al. in preparation

Im, M., Paek, G. S. H., Kim, J., Lim, G., & Gecko Team. 2023, in IAU Symposium, Vol. 363, Neutron Star Astrophysics at the Crossroads: Magnetars and the Multimessenger Revolution, ed. E. Troja & M. G. Baring, 207–210, doi: 10.1017/S1743921322000503

Ivezić, Ž., Kahn, S. M., Tyson, J. A., et al. 2019, ApJ, 873, 111, doi: 10.3847/1538-4357/ab042c

Karim, A., Schinnerer, E., Martínez-Sansigre, A., et al. 2011, ApJ, 730, 61, doi: 10.1088/0004-637X/730/2/61

Kennicutt, R. C., & Evans, N. J. 2012, ARA&A, 50, 531, doi: 10.1146/annurev-astro-081811-125610

Kewley, L. J., Dopita, M. A., Leitherer, C., et al. 2013, ApJ, 774, 100, doi: 10.1088/0004-637X/774/2/100

Kewley, L. J., Nicholls, D. C., & Sutherland, R. S. 2019, ARA&A, 57, 511, doi: 10.1146/annurev-astro-081817-051832

Kim, J., Im, M., Paek, G. S. H., et al. 2021, ApJ, 916, 47, doi: 10.3847/1538-4357/ac0446

Kim, J. H., Im, M., Lee, H., et al. 2024, in Society of Photo-Optical Instrumentation Engineers (SPIE) Conference Series, Vol. 13094, Ground-based and Airborne Telescopes X, ed. H. K. Marshall, J. Spyromilio, & T. Usuda, 130940X, doi: 10.1117/12.3019546

Knox, L., Song, Y.-S., & Zhan, H. 2006, ApJ, 652, 857, doi: 10.1086/508605

Koo, D. C. 1985, AJ, 90, 418, doi: 10.1086/113748

Kovač, K., Lilly, S. J., Cucciati, O., et al. 2010, ApJ, 708, 505, doi: 10.1088/0004-637X/708/1/505

Laigle, C., McCracken, H. J., Ilbert, O., et al. 2016, ApJS, 224, 24, doi: 10.3847/0067-0049/224/2/24

Laigle, C., Davidzon, I., Ilbert, O., et al. 2019, MNRAS, 486, 5104, doi: 10.1093/mnras/stz1054

Laur, J., Tempel, E., Tamm, A., et al. 2022, A&A, 668, A8, doi: 10.1051/0004-6361/202243881

Laureijs, R., Amiaux, J., Arduini, S., et al. 2011, arXiv e-prints, arXiv:1110.3193, doi: 10.48550/arXiv.1110.3193

Lilly, S. J., Le Fèvre, O., Renzini, A., et al. 2007, ApJS, 172, 70, doi: 10.1086/516589

Loh, E. D., & Spillar, E. J. 1986, ApJ, 303, 154, doi: 10.1086/164062

Mandelbaum, R. 2018, ARA&A, 56, 393, doi: 10.1146/annurev-astro-081817-051928

Mendes de Oliveira, C., Ribeiro, T., Schoenell, W., et al. 2019, MNRAS, 489, 241, doi: 10.1093/mnras/stz1985

Momcheva, I. G., Brammer, G. B., van Dokkum, P. G., et al. 2016, ApJS, 225, 27, doi: 10.3847/0067-0049/225/2/27

Moy, E., Barmby, P., Rigopoulou, D., et al. 2003, A&A, 403, 493, doi: 10.1051/0004-6361:20030245

Navarro-Gironés, D., Gaztañaga, E., Crocce, M., et al. 2023, arXiv e-prints, arXiv:2312.07581, doi: 10.48550/arXiv.2312.07581

Newman, J. A., & Gruen, D. 2022, ARA&A, 60, 363, doi: 10.1146/annurev-astro-032122-014611

Oke, J. B. 1974, ApJS, 27, 21, doi: 10.1086/190287

Paek, G. S. H., Im, M., Kim, J., et al. 2024, ApJ, 960, 113, doi: 10.3847/1538-4357/ad0238

Peimbert, M., Peimbert, A., & Delgado-Inglada, G. 2017, PASP, 129, 082001, doi: 10.1088/1538-3873/aa72c3

Renard, P., Siudek, M., Eriksen, M. B., et al. 2022, MNRAS, 515, 146, doi: 10.1093/mnras/stac1730

Rhodes, J., Nichol, R. C., Aubourg, É., et al. 2017, ApJS, 233, 21, doi: 10.3847/1538-4365/aa96b0

Ruppin, F., McDonald, M., Hlavacek-Larrondo, J., et al. 2023, ApJ, 948, 49, doi: 10.3847/1538-4357/acc38d

Saito, S., de la Torre, S., Ilbert, O., et al. 2020, MNRAS, 494, 199, doi: 10.1093/mnras/staa727

Salvato, M., Ilbert, O., & Hoyle, B. 2019, Nature Astronomy, 3, 212, doi: 10.1038/s41550-018-0478-0

Sánchez, C., Raveri, M., Alarcon, A., & Bernstein, G. M. 2020, MNRAS, 498, 2984, doi: 10.1093/mnras/staa2542

Sarrouh, G. T. E., Muzzin, A., Iyer, K. G., et al. 2024, ApJL, 967, L17, doi: 10.3847/2041-8213/ad43e8

Schaerer, D., & de Barros, S. 2009, A&A, 502, 423, doi: 10.1051/0004-6361/200911781

Schlegel, D. J., Finkbeiner, D. P., & Davis, M. 1998, ApJ, 500, 525, doi: 10.1086/305772

Sesar, B., Ivezić, Ž., Lupton, R. H., et al. 2007, AJ, 134, 2236, doi: 10.1086/521819

Simpson, C., Westoby, P., Arumugam, V., et al. 2013, MNRAS, 433, 2647, doi: 10.1093/mnras/stt940

Stabenau, H. F., Connolly, A., & Jain, B. 2008, Monthly Notices of the Royal Astronomical Society, 387, 12151226, doi: 10.1111/j.1365-2966.2008.13317.x

Stickley, N. R., Capak, P., Masters, D., et al. 2016, arXiv e-prints, arXiv:1606.06374, doi: 10.48550/arXiv.1606.06374

Stölzner, B., Joachimi, B., Korn, A., Hildebrandt, H., & Wright, A. H. 2021, A&A, 650, A148, doi: 10.1051/0004-6361/202040130

Taylor, E. N., Franx, M., van Dokkum, P. G., et al. 2009, ApJS, 183, 295, doi: 10.1088/0067-0049/183/2/295

The LSST Dark Energy Science Collaboration, Mandelbaum, R., Eifler, T., et al. 2018, arXiv e-prints, arXiv:1809.01669, doi: 10.48550/arXiv.1809.01669

Tonry, J. L., Stubbs, C. W., Lykke, K. R., et al. 2012, ApJ, 750, 99, doi: 10.1088/0004-637X/750/2/99

van Dokkum, P. G., Labbé, I., Marchesini, D., et al. 2009, PASP, 121, 2, doi: 10.1086/597138

Weaver, J. R., Kauffmann, O. B., Ilbert, O., et al. 2022, ApJS, 258, 11, doi: 10.3847/1538-4365/ac3078

Whitaker, K. E., Labbé, I., van Dokkum, P. G., et al. 2011, ApJ, 735, 86, doi: 10.1088/0004-637X/735/2/86

Williams, C. C., Tacchella, S., Maseda, M. V., et al. 2023, ApJS, 268, 64, doi: 10.3847/1538-4365/acf130

Withers, S., Muzzin, A., Ravindranath, S., et al. 2023, ApJL, 958, L14, doi: 10.3847/2041-8213/ad01c0

Wolf, C., Meisenheimer, K., Rix, H. W., et al. 2003, A&A, 401, 73, doi: 10.1051/0004-6361:20021513